

Energy transfer and budget analysis for transient process with operator-driven reduced-order model

Yuto Nakamura[†], Yuma Kuroda, Shintaro Sato, and Naofumi Ohnishi

Department of Aerospace Engineering, Tohoku University, Sendai, 980-8579, Japan

(Received xx; revised xx; accepted xx)

We present the possibility of energy transfer and budget analysis for transient flow using eigenmodes of the operator from the Navier–Stokes equation. We derive the energy transfer equation, which provides the energy budget for the eigenmodes, through the Galerkin projection of the equation using the bi-orthogonality of the eigenmodes and the adjoint mode. Energy budget and transfer analysis between modes were conducted for two-dimensional flow around a cylinder with eigenmodes growing or decaying from a steady flow. Using the linearized energy transfer equation and eigenmodes from global stability analysis, we identify the energy budget and spatial distribution that determine mode growth rates. Moreover, energy budget and transfer analysis are realized by considering the time evolution of the eigenmodes, even during the nonlinear development of the eigenmodes. By introducing time-varying dynamic mode decomposition with a phase-control strategy for multiple time-series datasets from numerical simulations of the phase-controlled initial flow, time-varying eigenmodes are extracted in the transient two-dimensional cylinder flow. With the extracted time-dependent modes and the derived energy transfer equations, the time evolution of the energy budget and spatial distribution of energy transfer can be computed until the eigenmodes developed from the steady field reach the post-transient periodic flow. From the time variation of the energy budget and the transfer distribution, the transient process of the cylinder flow can be characterized by the ratio of the magnitude of viscous diffusion for the eigenmode and energy transfer from the base flow.

Key words:

1. Introduction

Energy transfer due to the nonlinearity and viscous diffusion effects plays a fundamental role in fluid dynamics, governing phenomena such as vortex dynamics (Biswas & Buxton 2024; Freeman *et al.* 2023; Nakamura *et al.* 2025b), bifurcation instability (Noack *et al.* 2003; Deng *et al.* 2019), transient development (Zhong *et al.* 2025; Ballouz *et al.* 2024), and turbulence (Yamada & Ohkitani 1991; Nekkanti *et al.* 2025; Yeung & Schmidt 2025). Consequently, the budget of energy diffusion and transfer across different scales has been investigated through various approaches. Recent advances in data-driven science (Taira *et al.*

[†] Email address for correspondence: yuto.nakamura.t4@dc.tohoku.ac.jp

2017, 2020; Schmidt 2020; Towne *et al.* 2018; Schmid 2010; Fukami 2024) have enabled the extraction of coherent structures embedded in complex fluid flows and their decomposition into different scales. Furthermore, these advancements have cleared the energy transfer mechanisms between different scales. However, for transient flows undergoing nonlinear development, even the decomposition of flow structures into distinct scales remains a challenge. This paper advances the decomposition of transient flow into components of different scales, characterized by their frequencies, and analyzes the energy budget, considering both viscous diffusion and energy transfer.

Several modal decomposition methods exist for extracting coherent structures that help reveal energy transfer and the energy budget in fluid flow. One approach is to decompose the flow field into orthonormal modes. By projecting the governing equations onto a low-dimensional subspace spanned by these orthonormal modes, the viscous diffusion of the modes and their interactions can be studied. This approach is referred to as the Galerkin projection approach or Galerkin model (Noack & Eckelmann 1994*b*; Kunisch & Volkwein 2002), and the low-dimensional model is referred to as a reduced-order model (ROM). A well-known method for finding an orthonormal basis is proper orthogonal decomposition (POD) (Berkooz *et al.* 1993; Holmes 2012; Lumley 1967). POD extracts the most energetic modes from a flow dataset. Noack *et al.* (2003) demonstrated that the energy budget of each mode can be computed in a projection-based ROM using POD modes for the periodic flow around a two-dimensional cylinder. However, POD assumes a simple representation in terms of orthonormal bases, which means that a single mode may contain multiple frequency components. This limitation makes POD unsuitable for analyzing energy transfer between different frequencies.

Because of its ability to decompose into frequency-wise modes, decomposition in the spectral domain using wavelet analysis (Morlet *et al.* 1982; Goupillaud *et al.* 1984; Rinoshika & Rinoshika 2020; Ballouz *et al.* 2024) and Fourier decomposition (Freeman *et al.* 2024; Towne *et al.* 2018) are the most fundamental and widely used methods for energy transfer and budget analysis. Wavelet analysis has been used to analyze the energy budget and transfer related to high-frequency spectra in turbulent flows because of its ability to achieve high temporal resolution in the high-frequency domain (Yamada & Ohkitani 1991). In contrast, Fourier decomposition is effective in resolving the low-frequency region. Since the low-frequency components characterize the large-scale structure of the flow fields, Fourier decomposition is used to study the energy transfer related to the primary structure.

To extract large-scale coherent structures in turbulence, spectral proper orthogonal decomposition (SPOD) (Towne *et al.* 2018; Schmidt & Colonius 2020) has been developed to identify statistically significant modes at each frequency from Fourier modes. The original POD directly extracts the modes with the largest energy from the flow field dataset. However, the extracted modes may contain structures of different frequencies, which makes them unsuitable for analyzing energy transfer between different frequencies. SPOD addresses this limitation by performing POD on a frequency-by-frequency basis, thus ensuring that each mode corresponds to a single frequency component. The introduction of SPOD has significantly advanced energy transfer analysis by enabling the efficient extraction of dominant frequency components, even in turbulent flows.

Schmidt (2020) quantified the interaction between different frequencies, which drives energy transfer, using the bispectrum and proposed bispectral mode decomposition (BMD), which extracts the mode that maximizes the bispectrum and identifies the spatial regions where the interaction is strong. BMD has been applied to numerous flow situations, such as the wake flow of a turbine blade (Biswas & Buxton 2024), cylinder flow (Nakamura *et al.* 2025*b*), and jet flow (Nekkanti *et al.* 2025; Yeung & Schmidt 2025). The relationship between the spatial distribution of interactions, the bispectrum, and energy transfer has been discussed.

Although the bispectrum characterizes the strength of nonlinear interaction, it does not quantify the amount of energy transfer. To address this limitation, (Freeman *et al.* 2024, 2023) derived the Fourier-averaged Navier–Stokes equation (FANS), which is the Fourier decomposition of the Navier–Stokes equations, providing a way to physically interpret the bispectrum maximized by BMD. Based on FANS, the kinetic energy budget for the frequency component f_k ($k = 1, 2, \dots$) is given by

$$\text{Real} \left(\sum_{i=-\infty}^{\infty} - \int \hat{\mathbf{u}}_{f_k}^H (\hat{\mathbf{u}}_{f_k - f_i} \cdot \nabla) \hat{\mathbf{u}}_{f_i} d\mathbf{x} + \frac{1}{Re} \int \hat{\mathbf{u}}_{f_k}^H \nabla^2 \hat{\mathbf{u}}_{f_k} d\mathbf{x} \right) = 0, \quad (1.1)$$

where $\hat{\mathbf{u}}_{f_k}$ is the spectrum of the f_k -frequency component, and Real denotes the real part of a complex value. The first term represents the triadic energy transfer related to f_k , f_i , and $f_k - f_i$, while the second term represents the viscous diffusion effect. Through the first term, the frequency f_i component transfers energy to the f_k component. Computing the values of these terms from the Fourier modes, i.e., the spectrum reveals the energy transfer relationship between the f_k - and f_i -components, as well as the diffusion effect on the f_k -component.

Yeung *et al.* (2024) focused on the triadic energy transfer term obtained from FANS. They proposed triadic orthogonal decomposition (TOD) to extract the spatial structure that maximizes this triadic energy transfer term. By employing TOD, the frequency components that maximize their transfer relations and the local spatial structures in which energy transfer occurs are revealed for frequencies with arbitrary triadic relations. However, neither BMD, FANS, nor TOD are directly applicable to transiently developing flows since they all assume decomposition into Fourier modes. Applying mode decomposition optimized for weakly stationary flows to transient flows fails to capture the short-term behavior of the transient process (Schmid 2007). Because many natural and engineering flows exhibit transient development, extending energy transfer analysis to transient flows is crucial for understanding fluid dynamics.

To handle the triadic energy transfer between different frequencies in transient processes and viscous diffusion, a modal decomposition technique for the transient process is required. Amiri-Margavi & Babaee (2024) proposed treating transient flows by using the optimally time-dependent (OTD) mode for the flow field at each time and considering the time variation of modes. By enabling the time variation of the spatial distribution during the transient process, the transiently developing flow field can be optimally decomposed. The OTD formulation is similar to dealing with POD modes for a specific time in a transient process rather than decomposing it in the frequency domain. Ohmichi (2024) extended the variational mode decomposition, which can extract signals with variation in a specific frequency bandwidth, to flow fields and succeeded in decomposing transient flows into time-dependent modes with a specific center frequency.

Another approach for mode extraction is to consider the operators derived from the Navier–Stokes equations. Global stability analysis (GSA) (Noack & Eckelmann 1994a; Ohmichi 2014; Ohmichi & Yamada 2021; Ranjan *et al.* 2020) extracts global modes that can grow linearly from a base flow. To examine the eigenvalues of operators linearized around the base flow, the growth and decay of the corresponding eigenmodes and their frequencies are determined. Dynamic mode decomposition (DMD) (Schmid 2010, 2022; Tu 2013) is a method that can extract eigenmodes of a discrete dataset based on a linear operator, assuming that the dataset is time-advanced by the operator. Strictly speaking, DMD is not a method to extract eigenmodes from an operator, but DMD modes are comparable to eigenmodes of the operator. However, these methods are specialized for dealing with linear domains and are not suitable for direct application to transient processes because linear operators around a particular base flow cannot describe the nonlinear time evolution.

To decompose a transient process into eigenmodes of an operator, one approach is to consider the time variation of the base flow. Using a time-varying base flow, the operator can be linearized around the base flow at each time. Thus, in this case, the operator and the base flow are time-varying. For instance, time-varying DMD (Zhang *et al.* 2019) addresses the time variation of the operator by applying weights to the dataset, considering only certain times or using only data from specific time ranges. Stankiewicz *et al.* (2017) proposed a method to continuously interpolate the DMD modes of early development comparable to eigenmode from GSA with those of fully developed periodic flows. The change in base flow during the transient process is accomplished by correcting the mean field of stable periodic flow with the base flow at initial development (Noack *et al.* 2003), which is the steady-state flow satisfying the time-independent Navier–Stokes equation (Fornberg 1980). Note that rather than providing a model that aligns completely with the transient development of the actual flow, this is an approximation through interpolation. These methods can potentially describe the time variation of operators and their eigenmodes in transient processes. However, these methods are not extended to the energy transfer and budget analysis between different frequencies and viscous diffusion.

Resolvent analysis (Rolandi *et al.* 2024; Trefethen *et al.* 1993; Herrmann *et al.* 2021; Iwatani *et al.* 2023; Ballouz *et al.* 2024) is also a method for dealing with the development caused by energy amplification in transient flows. Considering the situation where the flow linearly develops from a specific base flow, resolvent analysis determines the optimal forcing that will maximize the energy amplification of the developed perturbation over a specific time span. An appropriate choice of time span and base flow can provide insights into energy transfer during the transient process. However, in practice, properly extracting the time-dependent variation in energy transfer during the growing process is difficult because the time-varying base flow and time span cannot be determined during the transient process.

Mode extraction based on time-varying operators can be extended to energy transfer analysis since the decomposition inherently relies on frequency. In this context, this paper addresses energy transfer and budget analysis using an ROM with time-varying operator eigenmodes in the transient process. Although the direction of the transfer analysis is similar to the energy budget analysis conducted by Noack *et al.* (2003) in POD-based ROM, our focus is on energy transfer analysis in the transient process of actual flow fields and the construction of an operator-based approach. A projection-based Galerkin model utilizing the eigenmodes of the operator and the bi-orthogonality between DMD modes and their adjoint modes (Tu 2013) has been proposed by Zhang & Wei (2017). Thus, this model is highly suitable for energy transfer and budget analysis for time-varying operator eigenmodes.

This paper explores the possibility of energy transfer analysis using operator eigenmodes with the adjoint-based Galerkin model and analyzes the energy transfer of transient flows. The manuscript is organized as follows. Section 2 describes the preparation strategy for the dataset used in mode extraction. This dataset is prepared through numerical simulations and incorporates time-stepping GSA (Ohmichi 2014; Ranjan *et al.* 2020). Additionally, a novel method is introduced for efficiently extracting modes from time-varying operators in transient flows. Section 3 derives a low-dimensional model based on the eigenmodes of the operators and formulates energy transfer equations for analyzing the energy transfer and budget of transient flows. Section 4 deals with linear processes in which modes grow or decay from the steady field in two-dimensional cylinder flow covered by the GSA. The energy transfer analysis, using the equations developed in section 3, is applied to these linearly growing modes. Section 5 extends the analysis to nonlinear mode growth, investigating energy transfer and budget in flows that grow beyond the linear region around the steady flow. Section 6 summarizes the main findings of this study.

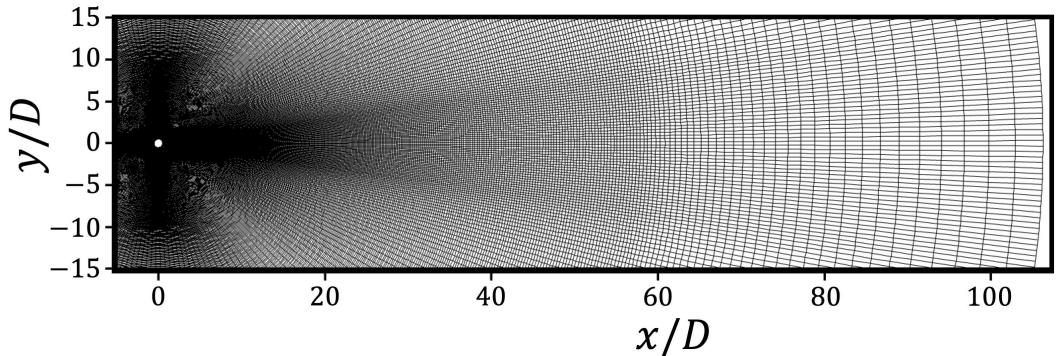


Figure 1: Computational grid around a circular cylinder.

2. Data preparation

2.1. Numerical method for solving governing equation

The flow around a circular cylinder was obtained from a numerical simulation of the incompressible Navier–Stokes equations. The governing equations are presented below.

$$\nabla \cdot \mathbf{u} = 0, \quad (2.1)$$

$$\frac{\partial \mathbf{u}}{\partial t} = -(\mathbf{u} \cdot \nabla) \mathbf{u} - \frac{1}{\rho} \nabla p + \frac{1}{Re} \nabla^2 \mathbf{u}. \quad (2.2)$$

where \mathbf{u} represents the velocity vector (bold symbols represent vectors), p is the pressure, and ρ is the fluid density.

The governing equations are solved by the fractional step method proposed by Le & Moin (1991). The time step size is determined based on our previous validation (Nakamura *et al.* 2024, Kobe, Japan). The second-order central difference (Kajishima & Taira 2017) and the QUICK method (Leonard 1979) were used for evaluating the spatial differences. The details of these numerical procedures are described in the Nakamura *et al.* (2024).

The computational mesh is shown in figure 1. The grid convergence is provided in Appendix A. The far-field boundary of computational meshes is extended up to $100D$, which is used to ensure that the numerical results are not affected by the far boundary (Kumar & Mittal 2006). In the wall-normal direction, the number of grids was 240. In the wall-parallel direction, the number of grids was 590. The height of the first layer next to the cylinder was set at $1.0 \times 10^{-3}D$ based on the DNS of Jiang & Cheng (2017).

2.2. GSA with time-stepping approach

The GSA is a practical approach to investigating the global instability in the base flow fields. From the perspective of the Hopf bifurcation behind a cylinder, base flow represents steady fields, and the global instability leads to the growing or decaying perturbation for the wake Karman vortex. The GSA considers time evolution of disturbances $\tilde{\mathbf{u}}$ by the Navier–Stokes equations around a base flow

$$\frac{d\tilde{\mathbf{u}}}{dt} = A\tilde{\mathbf{u}}, \quad (2.3)$$

where A denotes the operator around a base flow. The GSA aims to find the eigenvectors of matrix A . This study uses matrix-free GSA, which is referred to as a time-stepping approach (Ohmichi 2014; Ranjan *et al.* 2020). This method approximates the matrix A from the time evolution of the flow field with disturbances added to the base flow using numerical simulation.

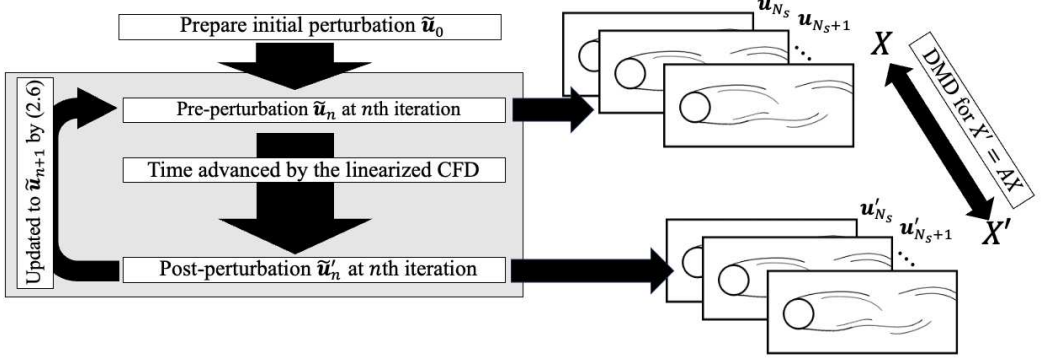


Figure 2: Schematic of time-stepping GSA using DMD.

A disturbance $\tilde{\mathbf{u}}_0$ is initially prepared by

$$\tilde{\mathbf{u}}_0 = \epsilon_0 |\mathbf{u}_\Delta| \frac{\mathbf{r}_0}{|\mathbf{r}_0|}, \quad (2.4)$$

where $|\cdot|$ represents the norm of the vector, \mathbf{u}_Δ is the base flow, \mathbf{u}_0 is the random disturbance, and ϵ_0 is a parameter that can be set to any value, representing the ratio of the baseflow and disturbance norms. The parameter dependence is provided in Appendix B. The flow field at $t_0 + \Delta T$ after a time progression by the numerical simulation is presented below

$$\mathbf{u}'_0(t_0 + \Delta T) = A'(\mathbf{u}_\Delta + \tilde{\mathbf{u}}_0), \quad (2.5)$$

where A' represents the temporal evolution matrix of numerical simulation, $\mathbf{u}'_n(t_n)$ is the flow field at t_n , t_0 is initial time. To collect data that approximate matrix A , we iteratively compute the time progression of the flow field with disturbances added to the base flow. For the n th iteration ($n > 1$), the disturbance $\tilde{\mathbf{u}}_n$ to the base flow is computed from the flow field of $n - 1$ th iteration presented below

$$\tilde{\mathbf{u}}_n = \epsilon_0 |\mathbf{u}_\Delta| \frac{\mathbf{u}'_{n-1} - \mathbf{u}_\Delta}{|\mathbf{u}'_{n-1} - \mathbf{u}_\Delta|}. \quad (2.6)$$

The eigenvectors of matrix A can be computed by applying DMD to the following matrices

$$X = [\mathbf{u}_{N_s}, \mathbf{u}_{N_s+1}, \dots, \mathbf{u}_{M+N_s-1}] \in \mathbb{R}^{N \times M}, \quad (2.7)$$

$$X' = [\mathbf{u}'_{N_s}, \mathbf{u}'_{N_s+1}, \dots, \mathbf{u}'_{M+N_s-1}] \in \mathbb{R}^{N \times M}. \quad (2.8)$$

where N_s is the starting position of the DMD data and is set to remove the effect of snapshots with initial disturbance, and M is the number of snapshots. The DMD-based mode extraction in the time-stepping GSA is proposed by Ranjan *et al.* (2020). In this study, N_s set to $150D/(U_{\text{inf}}\Delta T)$. M is set such that $N_s M - 1 = 50/(U_{\text{inf}}\Delta T)$ based on Nakamura *et al.* (2024).

2.3. DMD for mode extraction

DMD was proposed by Schmid (2010) to extract coherent structures from time series data of flow fields. This study computes eigenmodes from matrices X and X' obtained by time-stepping GSA based on an exact DMD algorithm (Tu 2013). The eigenmodes of matrix A are computed from X and X' as

$$A = X'X^\dagger, \quad (2.9)$$

where the superscript \dagger denotes the Moore–Penrose pseudoinverse. In the numerical processing, X is approximated by singular value decomposition (SVD)

$$X \approx U_r S_r V_r^T, \quad (2.10)$$

where U_r and V_r are the left and right singular vectors, respectively, S_r is the diagonal matrix with non-negative diagonal elements (the singular values of X). The matrix is approximated by

$$\tilde{A} = U_r^T X' V_r S_r^{-1}, \quad (2.11)$$

where \tilde{A} is low-rank approximation of A , thus, $\tilde{A} = U_r^T A U_r$.

The eigenvalue of matrix \tilde{A} represents the temporal evolution of corresponding eigenvectors (eigenmode). The frequency and the growth rate are computed from

$$f_k = \frac{\text{Imag}\{\log(\lambda_k)\}}{2\pi\Delta T}, \quad (2.12)$$

$$\sigma_k = \frac{\text{Real}\{\log(\lambda_k)\}}{\Delta T}, \quad (2.13)$$

where $\text{Real}(\cdot)$ and $\text{Imag}(\cdot)$ represent the real and imaginary parts of the complex values, respectively, and λ_k is the eigenvalue of \tilde{A} corresponding to the k th eigenmode. In this paper, we denote the eigenmode for frequency f_k by $\boldsymbol{\varphi}_{f_k}$. In the exact DMD, the eigenmodes $\boldsymbol{\varphi}_{f_k}$ is computed from the eigenmodes $\tilde{\boldsymbol{\varphi}}_{f_k}$ of \tilde{A} as follows

$$\boldsymbol{\varphi}_{f_k} = X' V_r S_r^{-1} \tilde{\boldsymbol{\varphi}}_{f_k}. \quad (2.14)$$

In this paper, f_k is indexed from $k = 1$ in decreasing order of $|f_k|$, and negative frequency is denoted by f_{-k} .

2.4. Mode extraction method for transient process using phase control

We extend time-stepping GSA to detect the nonlinear development of growth modes from steady fields. In the first iteration of the time-stepping method, the mode $\boldsymbol{\varphi}_{f_l}(\mathbf{x})$ with the largest growth rate is substituted for the random disturbance. Note that in the two-dimensional cylinder case, the most amplified mode corresponds to the most dominant, lowest-frequency fluctuating component, i.e., $l = 1$. To provide perturbations to the developmental process, we introduce an initial temporal phase α ($0 \leq \alpha < 2\pi$). In summary, the initial flow field is given by

$$\mathbf{u}(\mathbf{x}, 0, \alpha) = \mathbf{u}_\Delta + \epsilon_0 |\mathbf{u}_\Delta| \{e^{i\alpha} \boldsymbol{\varphi}_{f_l}(\mathbf{x}) + e^{-i\alpha} \boldsymbol{\varphi}_{f_{-l}}(\mathbf{x})\}. \quad (2.15)$$

Because of the nonlinear development of $\boldsymbol{\varphi}_{f_l}$ and \mathbf{u}_Δ , we do not update the fluctuating field in equation (2.6), and the operator from CFD is not linearized. Thus, time series data of the flow field from initial conditions controlled by α are obtained as follows

$$\mathbf{u}(\mathbf{x}, 0, \alpha), \mathbf{u}(\mathbf{x}, \Delta T, \alpha), \mathbf{u}(\mathbf{x}, 2\Delta T, \alpha), \dots, \mathbf{u}(\mathbf{x}, t, \alpha), \dots, \quad (2.16)$$

Here, we consider the average fields $\mathbf{u}_\Delta(\mathbf{x}, t)$ over α , defined as follows

$$\mathbf{u}_\Delta(\mathbf{x}, t) = \frac{1}{2\pi} \int_0^{2\pi} \mathbf{u}(\mathbf{x}, t, \alpha) d\alpha. \quad (2.17)$$

By linearizing the operator A around the $\mathbf{u}_\Delta(\mathbf{x}, t)$, time-varying linearized operator $A(t)$ can be defined. Note that the initial operator $A(0)$ equals the operator in the time-stepping GSA around the steady flow. Using this time-varying operator, time-series data is

$$\tilde{\mathbf{u}}(\mathbf{x}, 0, \alpha), A(0)\tilde{\mathbf{u}}(\mathbf{x}, 0, \alpha), A(\Delta T)\tilde{\mathbf{u}}(\mathbf{x}, \Delta T, \alpha), \dots, A(t)\mathbf{u}(\mathbf{x}, t, \alpha), \dots, \quad (2.18)$$

where $\tilde{\mathbf{u}}(\mathbf{x}, t, \alpha)$ is

$$\tilde{\mathbf{u}}(\mathbf{x}, t, \alpha) = \mathbf{u}(\mathbf{x}, t, \alpha) - \mathbf{u}_\Delta(\mathbf{x}, t). \quad (2.19)$$

Now, we consider the eigenmode of the time-varying operator $A(t)$. In this case, the eigenmode is a function of \mathbf{x} and t . Thus, the $\mathbf{u}(\mathbf{x}, t, \alpha)$ is decomposed into the result in time-variation of $\mathbf{u}_\Delta(\mathbf{x}, t)$ and $\boldsymbol{\varphi}_{f_k}(\mathbf{x}, t)$ presented below

$$\mathbf{u}(\mathbf{x}, t, \alpha) = \mathbf{u}_\Delta(\mathbf{x}, t) + \sum_{f_k} \beta_{f_k}(t) e^{\sigma t + (2\pi f_k t - \alpha)i} \boldsymbol{\varphi}_{f_k}(\mathbf{x}, t), \quad (2.20)$$

where $\beta_{f_k}(t)$ represents the amplitude of $\boldsymbol{\varphi}_{f_k}(\mathbf{x}, t)$ corresponding to the flow field at that time. Note that, in this decomposition, frequency f_k and growth rate σ are also time-varying with the operator. These idea are similar to time-varying DMD (Zhang *et al.* 2019; Guan *et al.* 2024) and OTD decomposition (Zhong *et al.* 2025; Amiri-Margavi & Babaei 2024; Aitzhan *et al.* 2025).

In numericaly, we compute the time-series data of equation (2.20) with discretized α to j_{\max} points presented below

$$\alpha_j = 2 \frac{j-1}{j_{\max}} \pi. \quad (2.21)$$

Here, uniformly discretizing α enables mode extraction with a small number of j_{\max} . The decomposition for mode is realized by applying exact DMD for the time-varying matrix X and X' presented below

$$X(t) = [\mathbf{u}(\mathbf{x}, t, \alpha_1), \mathbf{u}(\mathbf{x}, t, \alpha_2), \dots, \mathbf{u}(\mathbf{x}, t, \alpha_{j_{\max}})] \in \mathbb{R}^{N \times j_{\max}}, \quad (2.22)$$

$$X'(t) = [\mathbf{u}(\mathbf{x}, t + \Delta T, \alpha_1), \mathbf{u}(\mathbf{x}, t + \Delta T, \alpha_2), \dots, \mathbf{u}(\mathbf{x}, t + \Delta T, \alpha_{j_{\max}})] \in \mathbb{R}^{N \times j_{\max}} \quad (2.23)$$

The schematic of this modal decomposition procedure is shown in figure 3. We refer to this method as time-varying DMD with phase controlling (tDMDpc).

Amplitude of eigenmode from tDMDpc β_{f_k} is computed as follows:

$$[b_\Delta(t, \alpha_j), b_{f_k}(t, \alpha_j), b_{f_k}^*(t, \alpha_j)] = [\mathbf{u}_\Delta, \boldsymbol{\varphi}_{f_k}(\mathbf{x}, t), \boldsymbol{\varphi}_{f_k}^*(\mathbf{x}, t)]^\dagger \mathbf{u}(\mathbf{x}, t, \alpha_j). \quad (2.24)$$

$$\beta_{f_k}(t) = \sum_{j=1}^{j_{\max}} \frac{|b_{f_k}(t, \alpha_j)|}{j_{\max}}$$

where $*$ represents the complex conjugate. In this paper, $\boldsymbol{\varphi}_{f_k}^\dagger$ is computed by preconditioning the QR decomposition.

3. Model reduction approach and derivation of energy transfer equation

3.1. General derivation of Galerkin model with bi-orthogonality

The Galerkin model has been treated as a model reduction approach for low-dimensional representations of dynamical systems undergoing Hopf bifurcations (Noack & Eckelmann 1994a). The concept of the Galerkin model is to reformulate the governing equations in a low-dimensional form by decomposing the solution into basis functions. This study adapts the eigenmodes of the operator as the basis function and the Galerkin model based on the adjoint mode model proposed by Zhang & Wei (2017). The velocity field is assumed to be represented by the operator eigenmode $\boldsymbol{\varphi}_{f_k}(\mathbf{x})$ presented below

$$\mathbf{u}(\mathbf{x}, t) = \mathbf{u}_\Delta(\mathbf{x}) + \sum_{k=-r}^r a_{f_k}(t) \boldsymbol{\varphi}_{f_k}(\mathbf{x}), \quad (3.1)$$

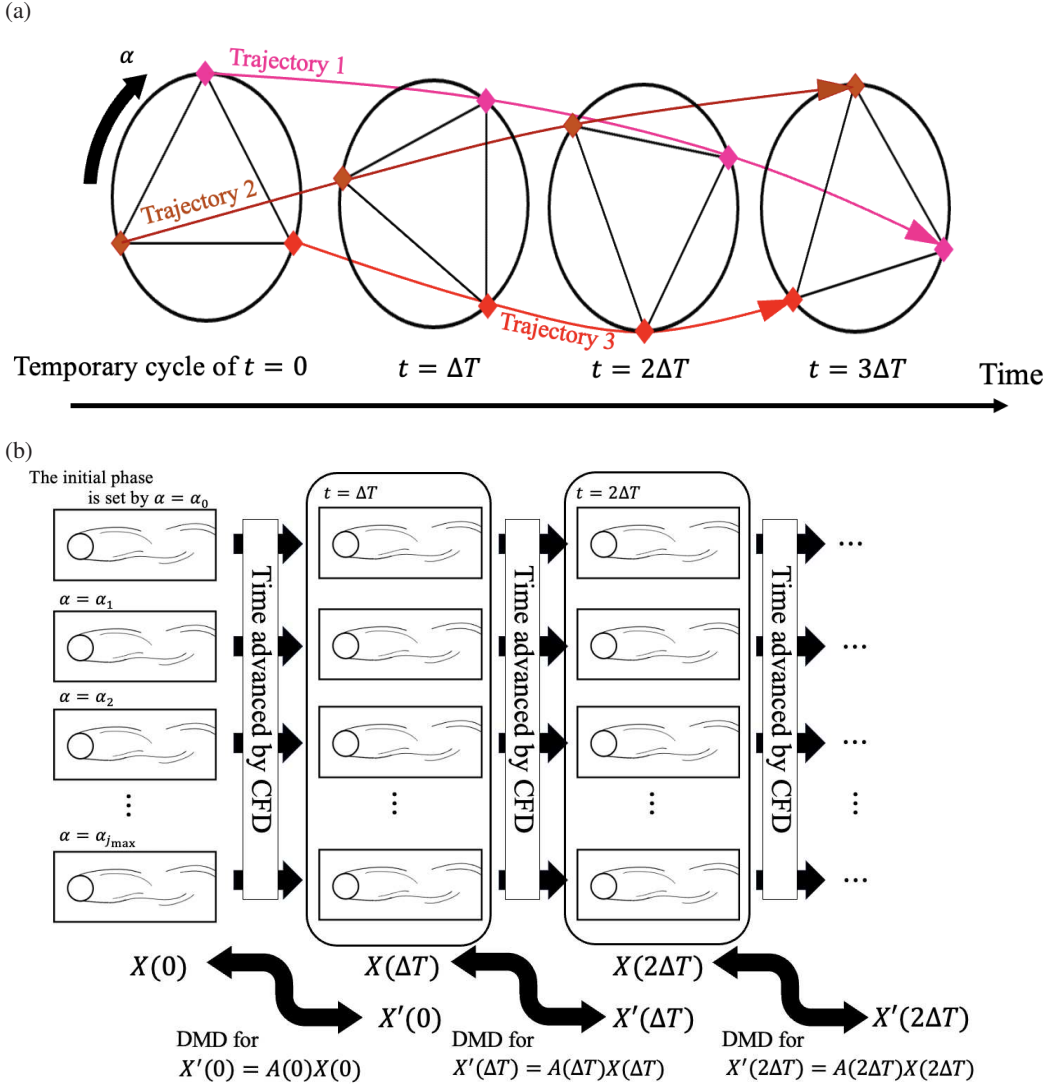


Figure 3: Schematic of tDMDpc. By changing the temporal phase of the mode in the initial flow and time progressing independently by CFD, a transient flow with different phases can be obtained.

where a_{f_r} represents the coupling coefficient for eigenmode which has f_k -frequency. Here, the $\varphi_{f_k}(\mathbf{x})$ does not depend on time. The \mathbf{u}_Δ needs to satisfy the boundary condition. The negative index is the negative frequency and satisfies the below

$$-f_k = f_{-k}, \quad (3.2)$$

$$a_{f_{-k}} = (a_{f_k})^*. \quad (3.3)$$

The negative frequency is required to represent the real-value velocity field by the complex-valued mode. The frequency f_0 means 0-frequency mode. When \mathbf{u}_Δ is different from the 0-frequency or time-average of the flow field, it is required to reproduce the oscillations around the mean flow (Noack *et al.* 2003).

The governing equation (2.2) is substituted into equation (3.1) as follows

$$\sum_{k=-r}^r \frac{da_{f_k}}{dt} \boldsymbol{\varphi}_{f_k} = - \sum_{i=-r}^r \sum_{j=-r}^r a_{f_i} a_{f_j} (\boldsymbol{\varphi}_{f_i} \cdot \nabla) \boldsymbol{\varphi}_{f_j} \quad (3.4)$$

$$- \sum_{i=-r}^r a_{f_i} \left\{ (\mathbf{u}_\Delta \cdot \nabla) \boldsymbol{\varphi}_{f_i} + (\boldsymbol{\varphi}_{f_i} \cdot \nabla) \mathbf{u}_\Delta + \frac{1}{Re} \nabla^2 \boldsymbol{\varphi}_{f_i} \right\} \quad (3.5)$$

$$- (\mathbf{u}_\Delta \cdot \nabla) \mathbf{u}_\Delta + \frac{1}{Re} \nabla^2 \mathbf{u}_\Delta - \frac{1}{\rho} \nabla p. \quad (3.6)$$

Here, we introduce an adjoint mode $\boldsymbol{\varphi}_{f_k}^{\text{ad}}$ whose inner product with the f_k -frequency eigenmode is unity and which is orthogonal to the other eigenmodes (biorthogonal), represented by the following equation

$$\langle \boldsymbol{\varphi}_{f_i}, \boldsymbol{\varphi}_{f_j}^{\text{ad}} \rangle = \delta_{ij}, \quad (3.7)$$

where δ_{ij} is the Kronecker delta. Note that the adjoint mode is the left eigenmode of A and can be computed from the right eigenmode of A^H , where the subscript H denotes the Hermitian transpose (Tu 2013). In equation (3.6), computing the inner product with the f_k -frequency adjoint mode, we obtain

$$\frac{da_{f_k}}{dt} = \sum_{i=-r}^r \sum_{j=-r}^r a_{f_i} a_{f_j} F_{f_i f_j f_k} + \sum_{i=-r}^r a_{f_i} G_{f_i f_k} + H_{f_k}, \quad (3.8)$$

where

$$F_{f_i f_j f_k} = - \langle (\boldsymbol{\varphi}_{f_i} \cdot \nabla) \boldsymbol{\varphi}_{f_j}, \boldsymbol{\varphi}_{f_k}^{\text{ad}} \rangle, \quad (3.9)$$

$$G_{f_i f_k} = \frac{1}{Re} \langle \nabla^2 \boldsymbol{\varphi}_{f_i}, \boldsymbol{\varphi}_{f_k}^{\text{ad}} \rangle - \langle (\mathbf{u}_\Delta \cdot \nabla) \boldsymbol{\varphi}_{f_i}, \boldsymbol{\varphi}_{f_k}^{\text{ad}} \rangle - \langle (\boldsymbol{\varphi}_{f_i} \cdot \nabla) \mathbf{u}_\Delta, \boldsymbol{\varphi}_{f_k}^{\text{ad}} \rangle, \quad (3.10)$$

$$H_{f_k} = \frac{1}{Re} \langle \nabla^2 \mathbf{u}_\Delta, \boldsymbol{\varphi}_{f_k}^{\text{ad}} \rangle - \langle (\mathbf{u}_\Delta \cdot \nabla) \mathbf{u}_\Delta, \boldsymbol{\varphi}_{f_k}^{\text{ad}} \rangle. \quad (3.11)$$

Note that the pressure term in the equation (3.6) is neglectable in the cylinder flow (Ma & Karniadakis 2002; Noack *et al.* 2005).

3.2. Derivation of global energy transfer equation

We derive an equation that describes the energy transfer relationship between modes of different frequencies. Considering a triadic of two or three frequencies, the frequencies that interact with each other have the following relationship

$$f_o \mp f_p \pm f_q = 0. \quad (3.12)$$

In the ROM, interaction between different frequencies occurs through the coefficients F and G . Thus, the coefficients for frequencies that are not in a triadic relationship are

$$F_{f_i f_j f_k} = 0 \quad (f_k \neq f_i + f_j), \quad (3.13)$$

$$G_{f_i f_k} = 0 \quad (f_k \neq f_i), \quad (3.14)$$

$$H_{f_k} = 0 \quad (f_k \neq 0). \quad (3.15)$$

Note that the term corresponding to the difference interaction must take the conjugate of the modes so that

$$F_{f_i f_j f_k} \neq F_{f_i f_{-j} f_k}, \quad (3.16)$$

$$G_{f_i f_k} \neq G_{f_{-i} f_k}. \quad (3.17)$$

This assumes that mode φ_{f_k} oscillates at frequency f_k . In this context, equation (3.6) is

$$\frac{da_{f_k}}{dt} = \sum_{i=\max(k-r, -r)}^{\min(k+r, r)} (a_{f_i} a_{f_{k-i}} F_{f_i f_{k-i} f_k}) + a_{f_k} G_{f_k f_k} \quad (k \neq 0), \quad (3.18)$$

$$\frac{da_{f_0}}{dt} = \sum_{i=-r}^r (a_{f_i} a_{f_{-i}} F_{f_i f_{-i} f_0}) + a_{f_0} G_{f_0 f_0} + H_0 \quad (k = 0). \quad (3.19)$$

Here, the summation $\sum_{i=\max(k-r, -r)}^{\min(k+r, r)}$ symbolically indicates that among the r frequencies, the nonlinear terms are summarized for frequencies in a triadic relationship with f_k .

To derive the energy transfer for the frequency f_k , we consider the time derivative of $|a_{f_k}|^2$. By mathematical deformation, we obtain

$$\frac{d}{dt} |a_{f_k}|^2 = a_{f_k}^* \frac{da_{f_k}}{dt} + a_{f_k} \frac{da_{f_k}^*}{dt} \quad (3.20)$$

$$= 2\text{Real} \left(a_{f_k}^* \frac{da_{f_k}}{dt} \right) \quad (3.21)$$

Therefore, the time derivative of energy satisfies the following equation

$$\frac{1}{2} \frac{d}{dt} |a_{f_k}|^2 = \sum_{i=\max(k-r, -r)}^{\min(k+r, r)} \text{Real}(a_{f_i} a_{f_{k-i}} a_{f_k}^* F_{f_i f_{k-i} f_k}) + \text{Real}(G_{f_k f_k}) |a_{f_k}|^2. \quad (3.22)$$

Here, since $|a_{f_k}|^2$ represents the integral amount of energy over the entire fields, equation (3.22) is the global energy transfer equation. Note that the first term of the right-hand side of equation (3.22) means the triadic interaction of f_i , f_k , and f_{k-i} . The second term includes the diffusion effect and interaction with 0-frequency mode.

3.3. Around the steady flow

In the Hopf bifurcation, the flow field comprises a steady base flow and oscillators of frequency $f_1 \approx 0.1$. Hence, the reduction to the most straightforward system for Hopf bifurcation begins with expressing the velocity field as

$$\mathbf{u}(\mathbf{x}, t) = \mathbf{u}_\Delta(\mathbf{x}) + a_{f_1}(t) \boldsymbol{\varphi}_{f_1}(\mathbf{x}) + a_{f_{-1}}(t) \boldsymbol{\varphi}_{f_{-1}}(\mathbf{x}). \quad (3.23)$$

where $\boldsymbol{\varphi}_{f_1}(\mathbf{x})$ does not depend on time since linear growth from the steady field is assumed. Since the nonlinear term is negligible due to linearization around the steady field, the dynamical system reduced by the Galerkin model is summarized below.

$$\frac{da_{f_1}}{dt} = a_{f_1} G_{f_1 f_1}. \quad (3.24)$$

Thus, frequency and growth rate of a_{f_1} is

$$\sigma_{f_1} = \text{Real}(G_{f_1 f_1}) \quad (3.25)$$

$$f_1 = \frac{\text{Imag}(G_{f_1 f_1})}{2\pi}. \quad (3.26)$$

The global energy transfer equation is

$$\frac{d}{dt} |a_{f_1}|^2 = 2\text{Real}(G_{f_1 f_1}) |a_{f_1}|^2 = 2\sigma_{f_1} |a_{f_1}|^2. \quad (3.27)$$

Generally, the following Landau equations describe the dynamical system of the Hopf bifurcation

$$\frac{dB}{dt} = \sigma B - B^3, \quad (3.28)$$

$$\frac{d\theta}{dt} = \omega - bB^2, \quad (3.29)$$

where B denotes the amplitude of the oscillator ($|a_{f_i}|$), σ is the growth rate of the oscillator at the equilibrium point, and θ is the oscillator's phase. In the context of the Landau equation, the square amount of the amplitude is

$$\frac{dB^2}{dt} = 2B \frac{dB}{dt} = 2\sigma B^2 - 2B^4, \quad (3.30)$$

A comparison of the equation for the squared amplitude derived from the Landau equation with the global energy transfer equation (3.27) shows that the transfer equation has no fourth-order term for the amplitude. The fourth-order term in equation (3.30) has the effect of suppressing amplitude amplification due to its negative coefficient. This term stabilizes the oscillator at a specific limit cycle when it leaves the equilibrium point. Hence, the absence of a fourth-order term in the global energy transfer equation leads to energy divergence in the reduced dynamical system. Noack *et al.* (2003) showed that correcting the steady field with oscillator amplification can suppress the divergence of the amplitude (mean-field correction). However, since the amplitude is close to 0 around the steady field, the effect of the fourth-order term is negligible. This indicates that the global energy transfer equation is a valid approximation at the steady field.

Moreover, the comparison of the coefficients of the second-order terms leads to the simple conclusion that the growth rate is equal to $\text{Real}(G_{f_i f_i})$. When kinetic energy is defined as $\mathbf{u}^T \mathbf{u}$, energy transfer represents $2\sigma \mathbf{u}^T \mathbf{u}$. That is, once \mathbf{u} is energized, the dynamical system acts as an amplifier of \mathbf{u} 's oscillation. Hence, the change in sign of the growth rate pre and post-critical Re indicates a shift in the energy transfer direction. This simple conclusion connects dynamical systems and fluid dynamics. Note that for the structure that first transfers energy to \mathbf{u} , an approach based on the adjoint GSA (Giannetti & Luchini 2007; Luchini & Bottaro 2014; Ohmichi & Yamada 2021) or resolvent analysis is a reasonable choice.

3.4. For transient flow

We derive the energy transfer equation considering the time variation of mode and frequency. Taking into account the time variation of the mode, equation (3.1) becomes

$$\mathbf{u}(\mathbf{x}, t) = \mathbf{u}_\Delta(\mathbf{x}, t) + \sum_{k=-r}^r a_{f_k} \boldsymbol{\varphi}_{f_k}(\mathbf{x}, t). \quad (3.31)$$

where, for $k = 0$, $a_{f_k} = 0$ since the time variation of the base flow (0-frequency mode) is already accounted for by $\mathbf{u}_\Delta(\mathbf{x}, t)$. In this case, the time derivative term of the mode is required because

$$\frac{d}{dt}(a_{f_k} \boldsymbol{\varphi}_{f_i}) = \boldsymbol{\varphi}_{f_i} \frac{da_{f_k}}{dt} + a_{f_k} \frac{d\boldsymbol{\varphi}_{f_i}}{dt}. \quad (3.32)$$

In this manner, equation (3.8) is

$$\frac{da_{f_k}}{dt} = \sum_{i=-r}^r I_{f_k f_i} a_{f_i} + J_{f_k} + \sum_{i=-r}^r \sum_{j=-r}^r a_{f_i} a_{f_j} F_{f_i f_j f_k} + \sum_{i=-r}^r a_{f_i} G_{f_i f_k} + H_{f_k}, \quad (3.33)$$

where

$$I_{f_k f_i} = -\left\langle \frac{d\boldsymbol{\varphi}_{f_i}}{dt}, \boldsymbol{\varphi}_{f_k}^{\text{ad}} \right\rangle, \quad (3.34)$$

$$J_{f_k} = -\left\langle \frac{d\mathbf{u}_\Delta}{dt}, \boldsymbol{\varphi}_{f_k}^{\text{ad}} \right\rangle. \quad (3.35)$$

We introduce the dynamic orthogonality condition for 0-mean stochastic process proposed by Sapsis & Lermusiaux (2009) in the reduced-order model for time-varying partial differential equations,

$$\left\langle \frac{d\boldsymbol{\varphi}_{f_i}}{dt}, \boldsymbol{\varphi}_{f_k}^{\text{ad}} \right\rangle = 0. \quad (3.36)$$

The term of J_{f_k} represents the time variation of the 0-frequency field, which can be neglected for non-zero f_k . In this manner, equation (3.8) is

$$\frac{da_{f_k}}{dt} = \sum_{i=-r}^r \sum_{j=-r}^r a_{f_i} a_{f_j} F_{f_i f_j f_k} + \sum_{i=-r}^r a_{f_i} G_{f_i f_k} + H_{f_k} \quad (k \neq 0). \quad (3.37)$$

where $F_{f_i f_j f_k}$, $G_{f_i f_k}$, and H_{f_k} are also time-varying.

Therefore, for $k \neq 0$, equation (3.37) is equivalent to equation (3.8). By considering the dynamic triadic relationship at arbitrary times,

$$f_o(t) \mp f_p(t) \pm f_q(t) = 0, \quad (3.38)$$

the global energy transfer equation for time-varying modes ($k \neq 0$) becomes

$$-\frac{1}{2} \frac{d}{dt} |a_{f_k}|^2 + \sum_{i=\max(k-r, -r)}^{\min(k+r, r)} \text{Real}(a_{f_i} a_{f_{k-i}} a_{f_k}^* F_{f_i f_{k-i} f_k}) + \text{Real}(G_{f_k f_k}) |a_{f_k}|^2 = 0 \quad (3.39)$$

This represents a time-varying energy budget that considers the time variation of energy.

4. Energy transfer analysis around the steady flow

We analyze the energy transfer for decaying or growing modes using the global energy transfer equation linearized around a steady field for two-dimensional cylinder flow. In this section, we analyze time-independent modes derived from the equations linearized around a steady field. Thus, this section presents the energy transfer analysis for the GSA results.

4.1. GSA results

The time-stepping GSA was performed for the flow around a cylinder. The base flow is computed by imposing symmetry on $y = 0$ (Nakamura *et al.* 2025a). Figure 4 shows the streamwise velocity fields of the base flow at $Re = 100$. A recirculation region with negative streamwise velocity is formed in the cylinder wake. Many previous studies (Sen *et al.* 2009; Fornberg 1980) have reported that the recirculation region of the wake expands with increasing Re .

Figure 5 (a) shows the 0-lines of streamwise velocity for the base flow at various Re , which characterize the wake recirculation region. As the Reynolds number increases, the recirculation region becomes larger. Here, the length of the recirculation region, L_{recirc} , is defined as the x -position where the 0-line and $y = 0$ intersect, excluding the cylinder surface. Figure 5 (b) shows the relationship between L_{recirc} and Re . L_{recirc} increases linearly with Re , in close agreement with the results of Sen *et al.* (2009).

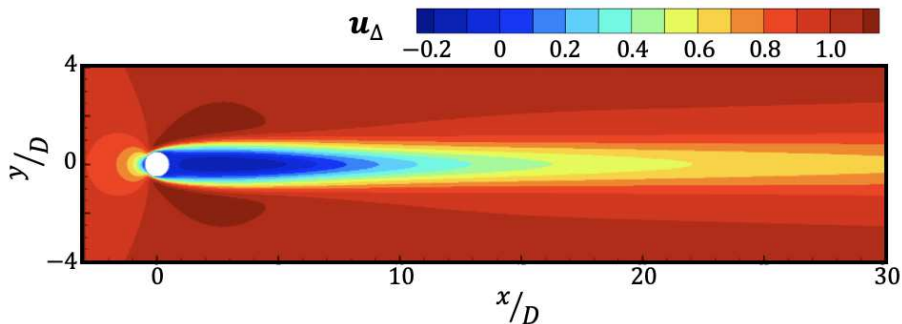


Figure 4: Streamwise velocity fields of the base flow at $Re = 100$. The base flow is obtained using the numerical technique of Nakamura *et al.* (2025a).

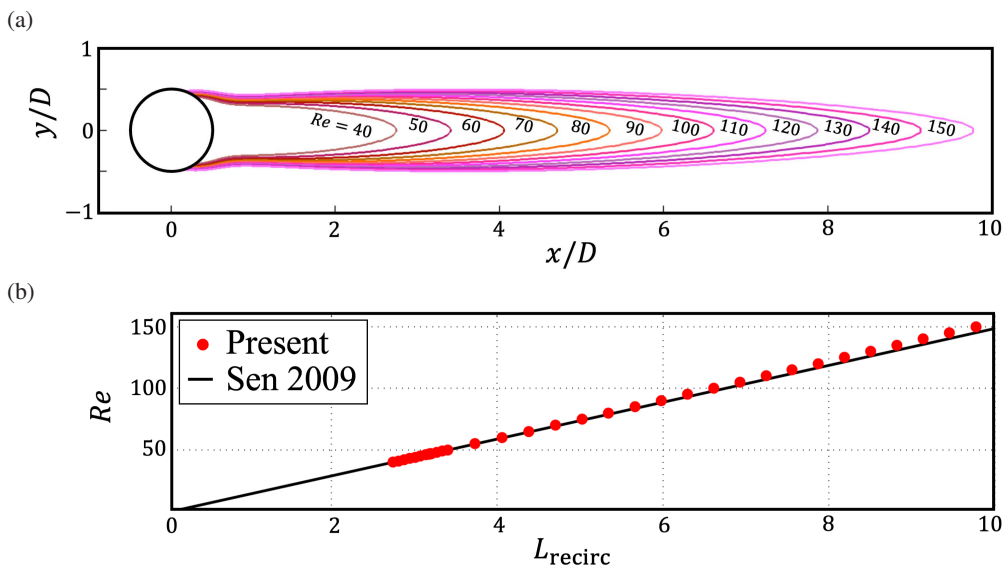


Figure 5: Base flow for various Re . (a) 0-line of the streamwise velocity component of the base flow (steady flow) at various Re . (b) The x -direction length of the recirculation region, L_{recirc} . The x -direction length of the 0 line expands linearly.

The GSA was performed using the obtained base flow \mathbf{u}_Δ . The details of the parameter choices in the time-stepping method are discussed in Appendix B. Figure 6 shows the modes with the most dominant eigenmode at $Re = 40, 60, 100,$ and 150 , obtained from the results of the GSA, along with the absolute value of the modes. The 0 line of the base flow for the same Re values is shown in the figure as a black line. In the case of cylinder flow, the most dominant mode has the lowest frequency, f_1 . Thus, the most unstable mode is referred to as φ_{f_1} . The spatial distribution of φ_{f_1} is asymmetric with respect to $y = 0$ for all Re cases. Focusing on the distribution around the 0 line of the base flow, asymmetric fluctuations exist vertically above and below the recirculation region enclosed by the 0 line. This represents the beginning of forming an asymmetric Kármán vortex from a symmetric recirculation region.

The distribution of absolute values of φ_{f_1} is in good agreement with Giannetti & Luchini (2007). For $Re > 60$, φ_{f_1} shows that the values become small sufficiently far from the cylinder. The peak value of $|\varphi_{f_1}|$ occurs at approximately $x/D \approx 10$, except for $Re = 40$. However, this position does not follow a monotonous trend with respect to Re .

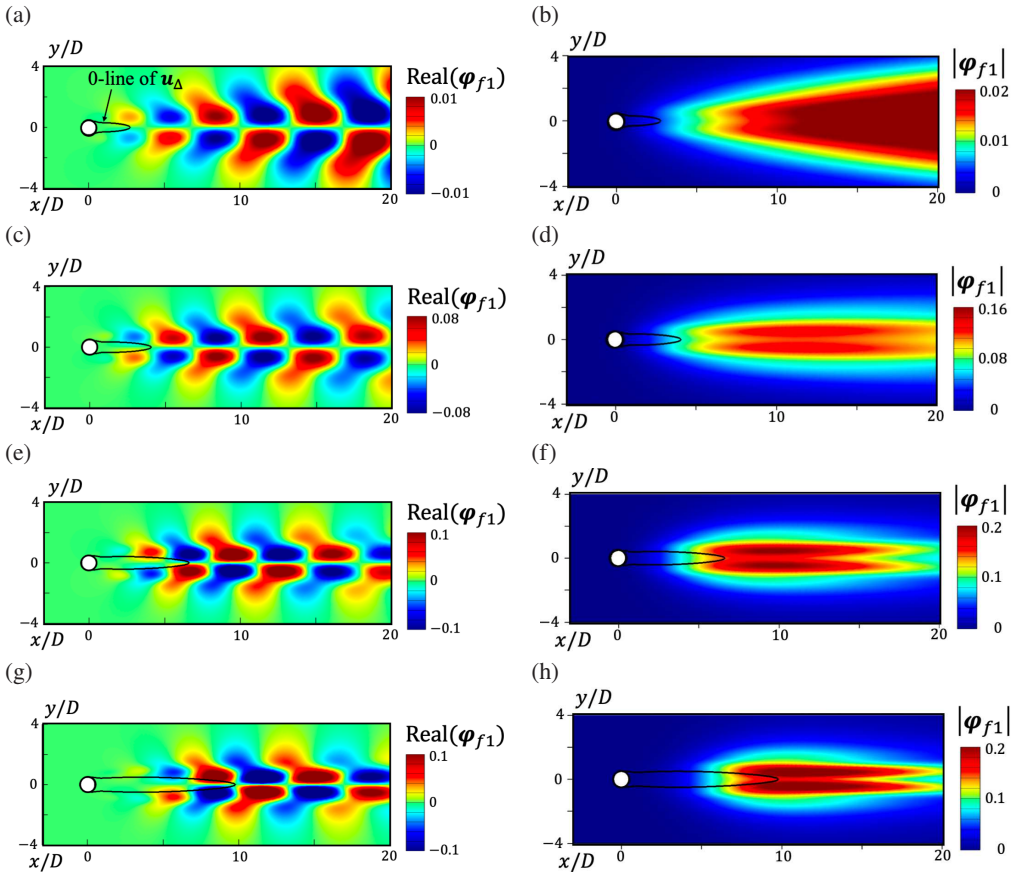


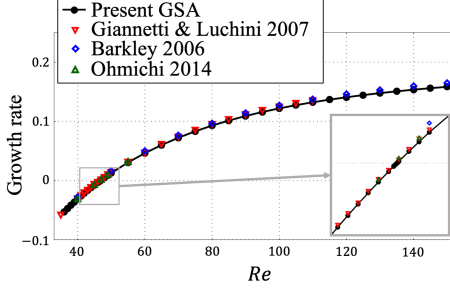
Figure 6: Spatial distribution of eigenmode φ_{f_1} and its absolute value: (a) and (b) $Re = 40$, (c) and (d) 60, (e) and (f) 100, and (g) and (h) 150. The black line indicates the 0 line of streamwise velocity from the base flow.

Figure 7 shows the growth rate of φ_{f_1} and the frequency f_1 at each Re . The growth rate monotonically increases with increasing Re , and the sign of the growth rate changes at $Re \approx 46.8$. The sign of the growth rate indicates whether the most unstable mode grows from the base flow, which implies the onset of a Hopf bifurcation. Thus, the critical Re is 46.8, which is quite similar to previous studies (Ohmichi 2014; Williamson 1996; Kumar & Mittal 2006; Barkley 2006; Giannetti & Luchini 2007). The frequency increases up to $Re = 65$ and then starts to decrease at that Re . This trend is consistent with previous studies. The frequency values are in close agreement with the results of Ohmichi (2014) but are slightly smaller than those of Barkley (2006) and Giannetti & Luchini (2007). The difference is possibly due to the GSA methodology, as Ohmichi's result is based on GSA using the time-stepping method (matrix-free method), while the other two results are obtained using the matrix method. As shown in Appendix B, the frequencies obtained by the time-stepping method are close to those obtained from numerical simulations. From this perspective, we conclude that the time-stepping method is reasonable.

4.2. ROM and energy transfer analysis

Galerkin-based ROM of the governing equations was conducted using the most unstable mode φ_{f_1} and the base flow \mathbf{u}_Δ at each Re . Using these modes, the growth rates in the ROM

(a)



(b)

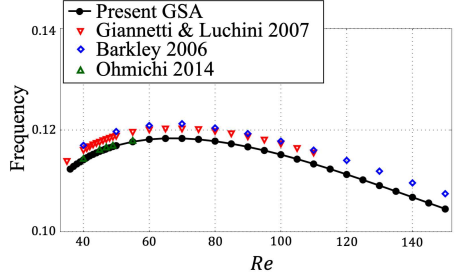
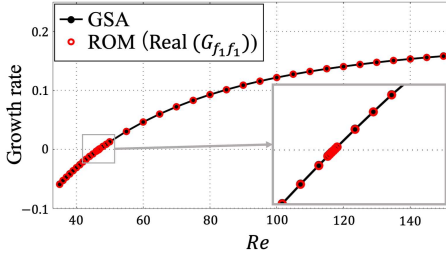


Figure 7: Result of time-stepping GSA with various Re , and comparison with previous work: (a) growth rate, (b) frequency.

(a)



(b)

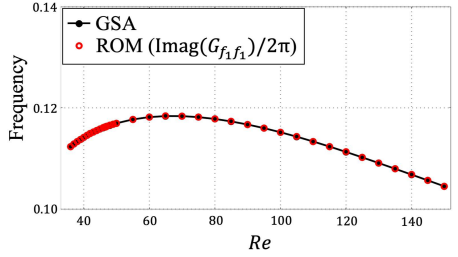


Figure 8: Comparison of growth rate and frequency between GSA and ROM, where growth rate and frequency of ROM is equal to $\text{Real}(G_{f_i f_i})$ and $\text{Imag}(G_{f_i f_i})/(2\pi)$. ROM closely approximates the growth rate and frequency of the eigenmode from GSA.

were computed based on equation (3.26). Figure 8 shows the growth rates and those obtained from GSA (indicated by the black line). The growth rates obtained from the ROM are in close agreement with the GSA results. Therefore, the ROM with base flow and unstable modes successfully reproduces the dynamical system around the base flow.

Here, we focus on the growth rate since it plays a significant role in the global energy transfer equation. From equation (3.26), the growth rate of the ROM is characterized by $\text{Real}(G_{f_i f_i})$. The $\text{Real}(G_{f_i f_i})$ is expressed as the summation of three terms shown in equation (3.11). The term $\frac{1}{Re} \langle \nabla^2 \varphi_{f_i}, \varphi_{f_i}^{\text{ad}} \rangle$ clearly represents the viscous diffusion term. In addition, the two nonlinear terms, $-\langle (\mathbf{u}_\Delta \cdot \nabla) \varphi_{f_i}, \varphi_{f_i}^{\text{ad}} \rangle$ and $\langle (\varphi_{f_i} \cdot \nabla) \mathbf{u}_\Delta, \varphi_{f_i}^{\text{ad}} \rangle$, also contribute to $G_{f_i f_i}$. From the momentum equation for the spectral energy budget, φ_{f_i} in the term $(\varphi_{f_i} \cdot \nabla) \varphi_{f_i}$ acts as the donor of energy to the recipient φ_{f_n} (Freeman *et al.* 2024; Yeung *et al.* 2024). Therefore, we now define the real parts of the three terms, considering their origins, as follows:

$$\mathcal{D}_{f_i} = \frac{1}{Re} \text{Real}(\langle \nabla^2 \varphi_{f_i}, \varphi_{f_i}^{\text{ad}} \rangle), \quad (4.1)$$

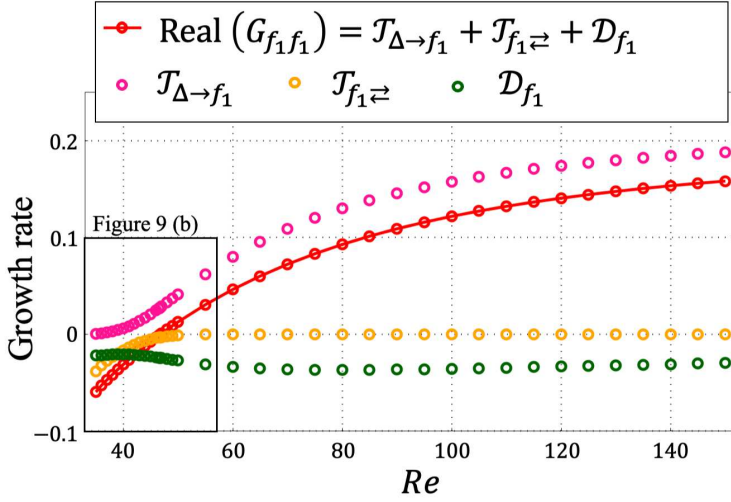
$$\mathcal{T}_{f_i \rightleftharpoons} = -\text{Real} \left\{ \langle (\mathbf{u}_\Delta \cdot \nabla) \varphi_{f_i}, \varphi_{f_i}^{\text{ad}} \rangle \right\}, \quad (4.2)$$

$$\mathcal{T}_{\Delta \rightarrow f_i} = -\text{Real} \left\{ \langle (\varphi_{f_i} \cdot \nabla) \mathbf{u}_\Delta, \varphi_{f_i}^{\text{ad}} \rangle \right\}, \quad (4.3)$$

where \mathcal{D} represents the diffusion term, \mathcal{T} is the transfer term, and the direction of the arrow in the subscript indicates the direction of energy transfer.

Figure 9 shows the values of the three terms computed numerically at each Re . Note that

(a)



(b)

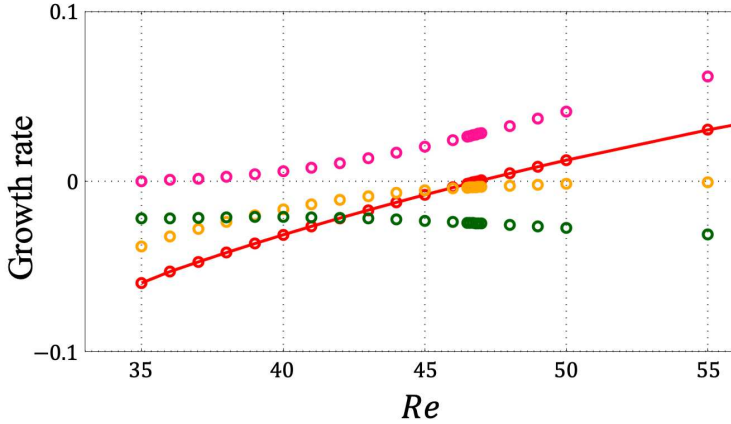


Figure 9: Individual plots of the three terms that comprise the ROM growth rate ($\text{Real}(G_{f_1 f_1})$): (a) overall view, (b) close-up view of bifurcation point.

the red line in the figure represents the growth rate of the ROM, which is the sum of the three terms, as shown by the red line in figure 8. For all Re cases, only $\mathcal{T}_{\Delta \rightarrow f_i}$ takes a positive value, indicating that $\mathcal{T}_{\Delta \rightarrow f_i}$ is the term that amplifies the energy of φ_{f_i} . The diffusion term \mathcal{D}_{f_i} is always negative and remains nearly constant regardless of the Re value. This is interesting because, in the straightforward property, \mathcal{D}_{f_i} has a coefficient of $1/Re$. This indicates that $\text{Real}(\langle \nabla^2 \varphi_{f_i}, \varphi_{f_i}^{\text{ad}} \rangle)$ increases with Re .

The term on $\mathcal{T}_{f_i \rightleftharpoons}$ is also negative at all Re cases. This is the self-transfer mechanism by which φ_{f_i} passes energy to φ_{f_i} , showing the decaying nature of φ_{f_i} itself. This self-decaying nature is also reported by Yeung *et al.* (2024) in the post-transient, periodic cylinder flow at $Re = 100$. When the Re is smaller than the critical Re , this self-decaying property is more pronounced, and for $Re < 39$, it is smaller than the diffusion term. Therefore, it seems necessary to investigate not only viscous diffusion effects but also self-decaying mechanisms to understand the stable dynamics before bifurcation.

Going back to the fact that the value of each of the three terms is computed by the spatial

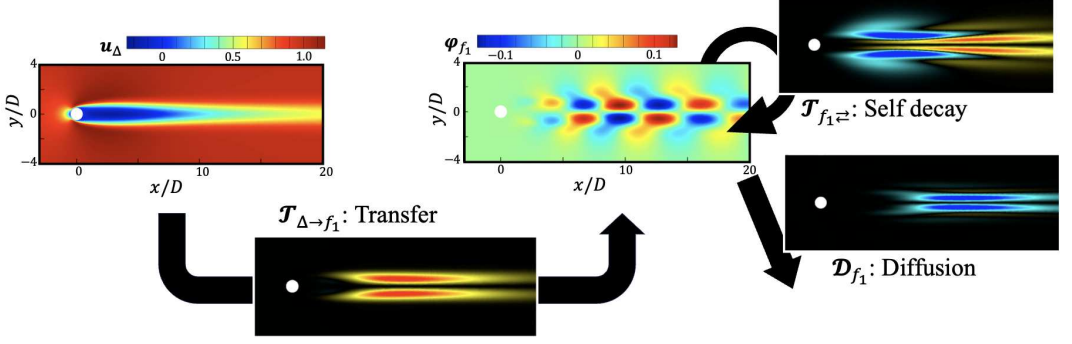


Figure 10: Diagram of energy transfer relationship of base flow u_Δ and φ_{f_1} in the case of linearized around the base flow. All contour map is the case of $Re = 100$, but this relationship is universal at least $Re = 35-150$ (see figure 9). The direction of the arrow indicates the signature of the integral value of the diffusion field and transfer field.

integration, the spatial distribution of the integrated function determines the value of each term. This motivates us to define the spatial fields that determine the values of the three terms as follows:

$$\mathcal{D}_{f_i} = \frac{1}{Re} \text{Real}(\nabla^2 \varphi_{f_i} \circ \varphi_{f_i}^{\text{ad}}), \quad (4.4)$$

$$\mathcal{T}_{f_i \rightleftharpoons} = -\text{Real}(u_\Delta \cdot \nabla) \varphi_{f_i} \circ \varphi_{f_i}^{\text{ad}}, \quad (4.5)$$

$$\mathcal{T}_{\Delta \rightarrow f_i} = -\text{Real}((\varphi_{f_i} \cdot \nabla) u_\Delta \circ \varphi_{f_i}^{\text{ad}}), \quad (4.6)$$

inspired by the interaction map of BMD (Schmidt 2020) and the transfer field of TOD (Yeung *et al.* 2024). Here, \circ denotes the elementwise product. We refer to the spatial field \mathcal{D}_{f_i} as the diffusion field, and $\mathcal{T}_{f_i \rightleftharpoons}$ and $\mathcal{T}_{\Delta \rightarrow f_i}$ as transfer fields.

Figure 10 shows a conceptual diagram at $Re = 100$, considering three spatial field distributions: \mathcal{D}_{f_1} , $\mathcal{T}_{f_1 \rightleftharpoons}$, and $\mathcal{T}_{\Delta \rightarrow f_1}$, as well as the energy transfer direction determined by the sign of their spatial integrations: \mathcal{D}_{f_1} , $\mathcal{T}_{f_1 \rightleftharpoons}$, and $\mathcal{T}_{\Delta \rightarrow f_1}$. Only $\mathcal{T}_{\Delta \rightarrow f_1}$ acts as an amplifier, supplying energy, while the other two act as energy dampers. Therefore, whether φ_{f_i} develops or not depends on the sum of these three terms. The diffusion field \mathcal{D}_{f_1} is entirely negative, whereas $\mathcal{T}_{\Delta \rightarrow f_1}$ shows an almost entirely positive distribution. In the field of $\mathcal{T}_{f_1 \rightleftharpoons}$, both positive and negative value regions exist.

Transfer fields and diffusion fields for $Re = 40, 60, 100$, and 150 are shown in figure 11. The 0-line of the streamwise velocity for the base flow is shown for $\mathcal{T}_{\Delta \rightarrow f_i}$, and the contour lines of $|\varphi_{f_1}|$ (see figure 6) are shown for the other fields by the white line. The diffusion field has a similar distribution to $|\varphi_{f_1}|$. This means that diffusion effects appear at all positions where fluctuations in the f_1 frequency component exist. The transfer fields $\mathcal{T}_{f_i \rightleftharpoons}$ exhibit a negative distribution near the cylinder and a positive distribution farther away from the cylinder, except for $Re = 40$. Compared to the distribution of $|\varphi_{f_1}|$, the distribution of $\mathcal{T}_{f_i \rightleftharpoons}$ switches between positive and negative values around the peak- x position of $|\varphi_{f_1}|$. These positive and negative regions cancel each other out, resulting in a net small negative transfer, $\mathcal{T}_{f_i \rightleftharpoons}$.

The transfer field $\mathcal{T}_{\Delta \rightarrow f_i}$ has a distribution along the backward direction of the recirculation region, bounded by the 0-line. This distribution is very similar to the sensitivity region where fluctuations are caused by the wake recirculation region, as reported by Ohmichi & Yamada (2021). Since $\mathcal{T}_{\Delta \rightarrow f_i}$ represents the energy transfer from the base flow to φ_{f_1} , the formation of φ_{f_1} originates from the recirculation region of the base flow. Therefore, the growth of

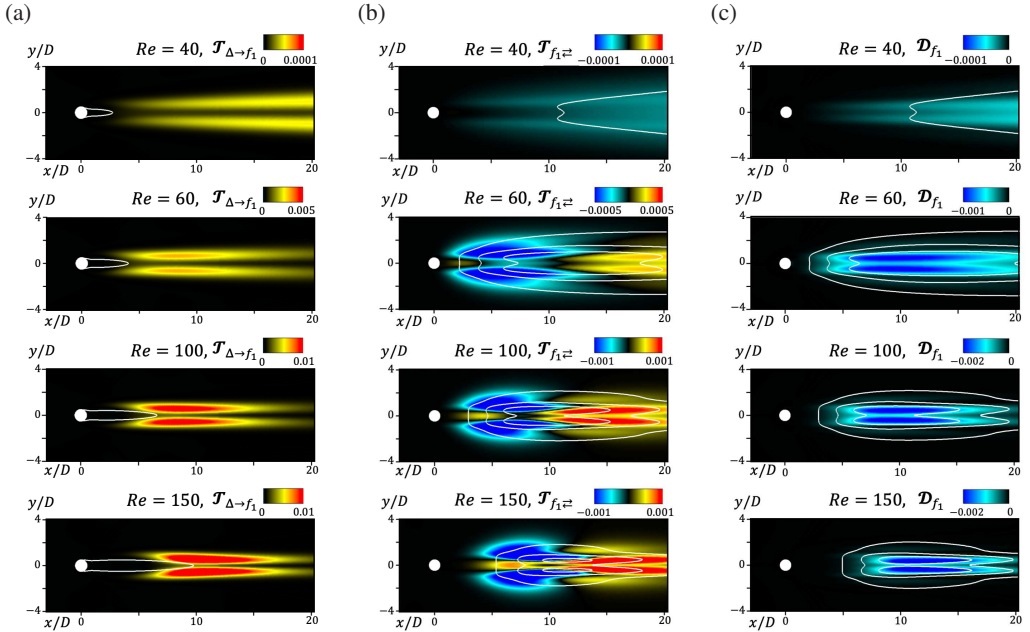


Figure 11: Spatial distribution of transfer fields and diffusion fields at $Re = 40, 60, 100,$ and 150 .

φ_{f_i} is driven by instability in the recirculation region of the wake. However, at $Re = 40$, this energy transfer is minimal, which is also evident from the integral value in figure 9. As Re increases, the length of the recirculation region also increases (see figure 5), making the wake recirculation more unstable and enhancing the energy transfer to φ_{f_i} .

We further investigate the relationship between the recirculation region and the location of transfer by $\mathcal{T}_{\Delta \rightarrow f_i}$. The recirculation region is characterized by L_{recirc} , as shown in figure 5. While there is no universal definition for the position of the transfer distribution, we define the most unstable position as the location where the transfer field $\mathcal{T}_{\Delta \rightarrow f_i}$ reaches its maximum value. Figure 12 illustrates the relationship between the maximum value position of the transfer field and the Re . For Re values below the bifurcation point, the maximum value of $\mathcal{T}_{\Delta \rightarrow f_i}$ is located much further downstream compared to that of Re values above the bifurcation point. However, the data for Re below the bifurcation point may contain numerical errors due to the very small energy transfer values, as shown for $Re = 40$ in figures 11 (a) and 9 (b).

Figure 12 (b) shows a close-up view of the post-bifurcation region. The x -position of the maximum value of the transfer field is smallest at $Re = 80$. As Re exceeds 80, the maximum-value position of the transfer field moves backward, and this movement follows a linear trend with respect to Re . Note that the discontinuity between adjacent Re values may be due to the coordinate discontinuity in the discretized grid. Figure 12 (c) shows the horizontal axis of figure 12 (b) adjusted to represent the recirculation-region length of the steady field for each Re . The linear relationship with the length of the recirculation region indicates that the primary transfer position moves as the length of the recirculation region shortens. Comparing this with the integral value of the transfer field $\mathcal{T}_{\Delta \rightarrow f_i}$ in Figure 9, the variation of $\mathcal{T}_{\Delta \rightarrow f_i}$ with respect to Re is smaller for $Re < 80$ than for $Re > 80$. In other words, as the energy transfer increases, the distribution of the transfer field moves closer to the recirculation region. Once energy transfer becomes significant enough, a transfer occurs near the recirculation region.

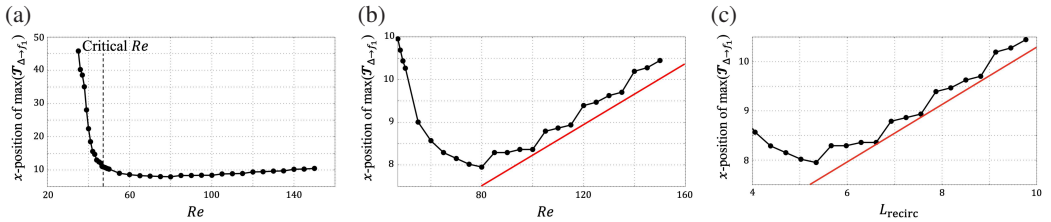


Figure 12: The x -position of the maximum value of the transfer fields $\mathcal{T}_{\Delta \rightarrow f_i}$ for various Re , (a) over a wide range of Re , (b) for post-critical Re , (c) for post-critical Re , but with the horizontal axis representing L_{recirc} .

5. Energy transfer and budget analysis for transient flow

The global energy transfer equation, linearized around the steady field, successfully captures the system's dynamics near the steady field obtained from GSA. This section extends the transfer analysis to a transient nonlinear development process beyond the linear growth from the steady field. In such cases, the linearized energy transfer equation (3.27) alone cannot fully describe the evolution of the solution (Stankiewicz *et al.* 2017). Moreover, both the spatial distribution and frequency of the modes change throughout the transient process. Therefore, we extract the variations in the spatial distribution and frequency of the modes during the transient process using tDMDpc and analyze the corresponding energy transfer dynamics. We aim to provide a more comprehensive understanding of how energy transfers between different frequency components as the flow evolves from the steady field to its post-transient state.

5.1. tDMDpc result for cylinder flow

The transient flow process around a cylinder is decomposed using tDMDpc, with modes obtained from time-stepping GSA around a steady field. The parameters ΔT and ϵ_0 are set to 0.1 and 0.001, respectively, the same values used in the time-stepping GSA. The initial perturbation fields at $\alpha = 0, \pi/2, \pi$ for $Re = 100$ are shown in figure 13. According to equation (2.15), the initial perturbation field at $\alpha = 0$ corresponds to the real part of the eigenmode, with its absolute value scaled by ϵ_0 . Thus, the spatial distribution in figure 13 (a) is identical to that in figure 6 (e). The initial perturbation field at $\alpha = \pi/2$ corresponds to the imaginary part of the eigenmode, also scaled by ϵ_0 . The initial perturbation field at $\alpha = \pi$ is equivalent to that at $\alpha = 0$ but with the sign inverted. Figure 13 (d) presents an overlay plot of the contours at 0.001 for the three fields. The spatial distribution of the perturbation field changes depending on the value of α , indicating that the phases of the oscillations differ.

The initial perturbation fields are prepared by varying the value of α under $j_{\text{max}} = 20$. Figure 14 shows the time variation of the transverse velocity at the wake position $(x/D, y/D) = (1, 0)$, computed from numerical simulations using the initial perturbation fields presented in figure 13. At $t = 0$, the velocity variation is too slight to be significant, but as time progresses, the velocity perturbation grows. Once the oscillation amplitude reaches a sufficiently large value, it stabilizes, and the flow field transitions to the post-transient state. A comparison of flow fields for different α values reveals that the oscillation phase shifts with respect to α . Therefore, time-series data of flow fields evolving from initial conditions with varying α provide the dataset of the development process with different temporal phases.

Using the time-series data of the flow field developed from $j_{\text{max}} = 20$ different α values, we computed the flow field averaged over α by (2.17) for snapshots at the same t . The number of snapshots, j_{max} , in tDMDpc, corresponds to the number of snapshots used for averaging and mode extraction. Therefore, a sufficiently large number of snapshots is required for accurate

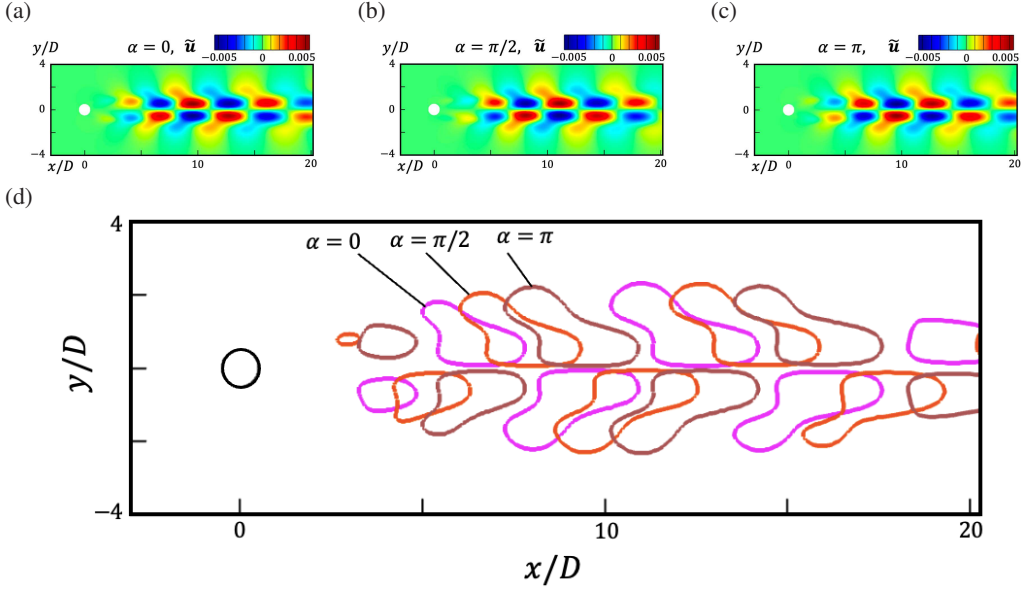


Figure 13: Initial perturbation fields of tDMDpc at $Re = 100$ (a) $\alpha = 0$, (b) $\alpha = \pi/2$, (c) $\alpha = \pi$, and (d) contour line of 0.001 at $\alpha = 0, \pi/2$, and π .

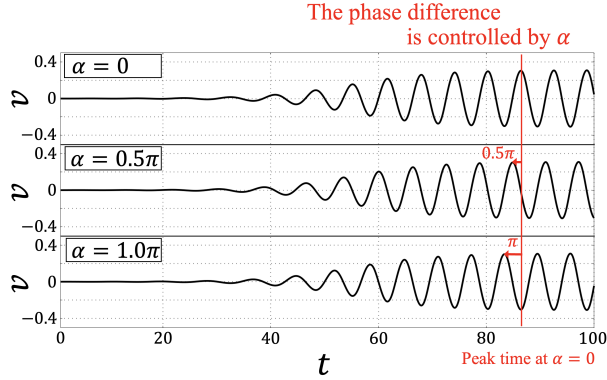


Figure 14: Time variation of transverse velocity component at $(x/D, y/D) = (1, 0)$ at $Re = 100$, with different α in tDMDpc. The temporal phase in the transient process can be controlled by α .

results. The convergence of the averaged fields and the modes extracted by tDMDpc with respect to $j_{\max} = 20$ is discussed in Appendix C. Figure 15 shows the 0-contour line of the streamwise velocity in the flow field averaged over α at various times. The length of the recirculation region, bounded by the 0-contour line, decreases as time progresses. Unlike the steady-state field, where the recirculation region increases linearly with Re , the recirculation region in the transient process does not vary linearly with time.

Time-varying modes and eigenvalues were extracted using tDMDpc from the time-series data obtained with $j_{\max} = 20$, as illustrated in the conceptual diagram in figure 3 (b). Figure 16 shows the distribution of the eigenvalues of tDMDpc at times $t = 30, 40, 55, 80$. These times were chosen based on the variation in the length of the recirculation region (see figure 15). The eigenvalues that exist on the unit circle, indicated by the black line in the figure,

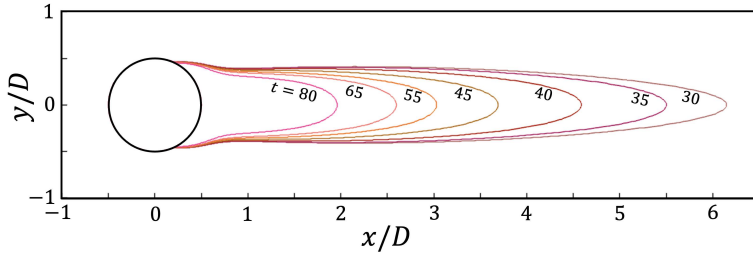


Figure 15: 0 line for streamwise velocity fields (recirculation region) at various times averaged over α in the tDMDpc. The Re is 100. As flow fields develop, the recirculation region and length to the x -direction becomes small.

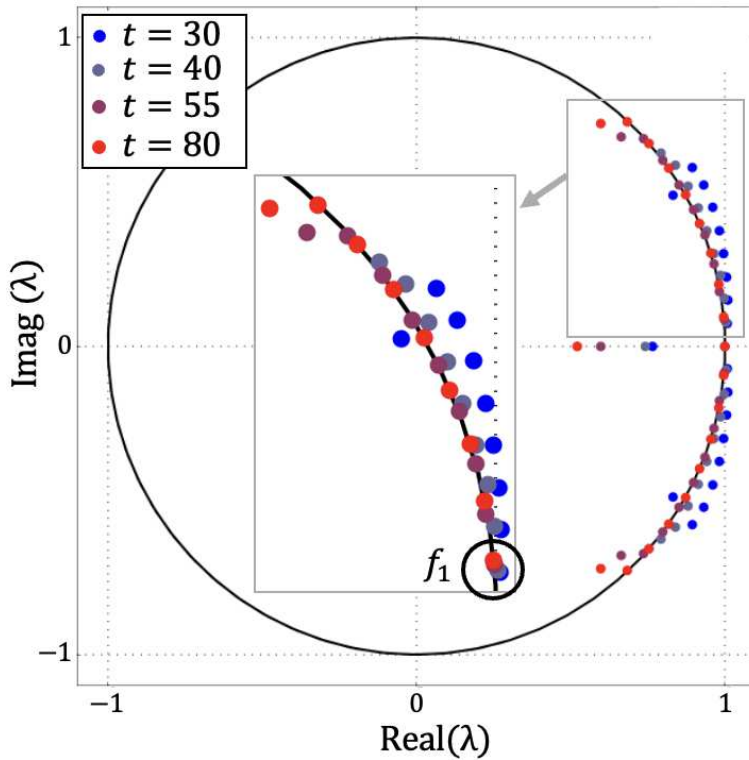


Figure 16: Eigenvalue distribution of tDMDpc at $Re = 100$. The black line represents the unit circle, which indicates the 0-growth rate. Flow fields become a stable state because the eigenvalue converges to the unit circle as time progresses.

correspond to a 0 growth rate. At $t = 30$ and 40 , a large number of eigenvalues are found outside the unit circle, indicating that the flow fields are growing. As time progresses, the eigenvalues concentrate around the unit circle, suggesting that the flow field converges to a stable quasi-steady state. The few eigenvalues located inside the unit circle are likely numerical errors near the outflow boundary.

The declination of each eigenvalue for the x -axis corresponds to the angular frequency. At $t = 30$, the eigenvalues with the lowest angular frequency, except for the 0-frequency, closely match the eigenvalues of the most unstable mode φ_{f_1} obtained from GSA. Therefore, the eigenvalues with the smallest angular frequency result from the nonlinear growing of the

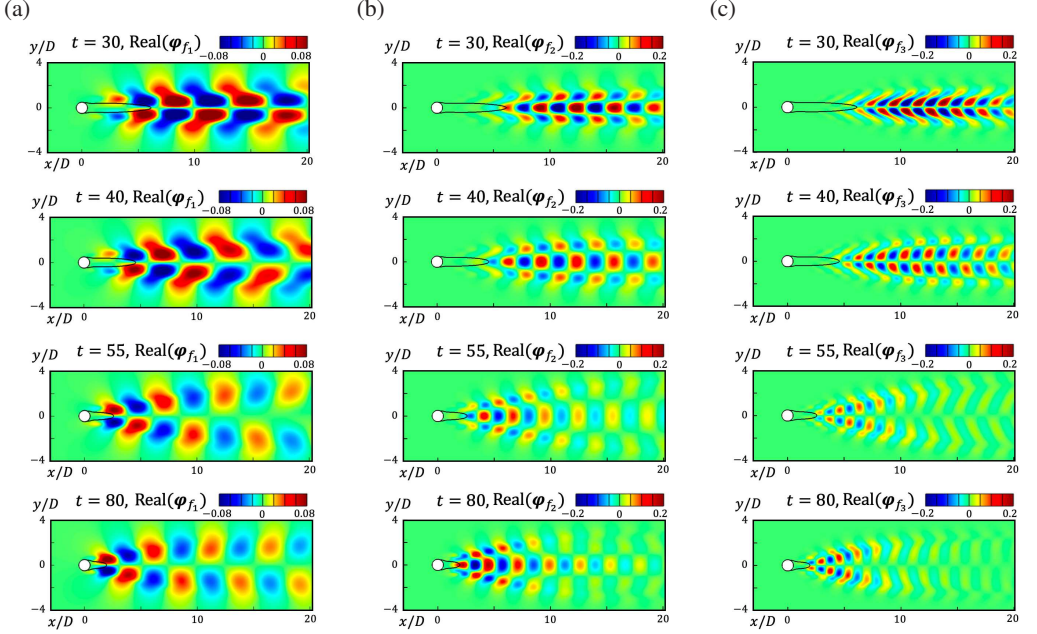


Figure 17: Time variation of eigen modes distribution from tDMDpc (a) most lowest-frequency f_1 (b) $f_2 = 2f_1$ (c) $f_3 = 3f_1$.

most unstable modes of GSA, which were used in the initial perturbation fields. Excluding numerical errors, it can be observed that the other frequencies correspond to harmonics of the f_1 frequency. This behavior arises from the nonlinear interaction between the φ_{f_1} mode and other finite-frequency modes, leading to the appearance of modes with frequencies $f_n = f_{n-1} + f_1$ for $n = 2, 3, \dots$.

Figure 17 presents the eigenmodes obtained from tDMDpc at frequencies $0.1 < f_1 < 0.2$, $f_2 = 2f_1$, and $f_3 = 3f_1$, extracted at $t = 30, 40, 55$, and 80 . The black line indicates the 0-contour line of the averaged fields over α simultaneously. For all three frequency components, as the recirculation region length decreases, the mode distribution gradually approaches that of a cylinder. At $t = 80$, the well-known mode distributions for periodic flow around a cylinder, as reported in several studies (Sato & Schmidt 2025; Akhtar 2008; Yeung *et al.* 2024; Noack *et al.* 2003; Taira *et al.* 2020; Tu 2013; Zhang & Wei 2017), are clearly visible. At $t = 30$, in the downstream position of the recirculation region, the magnitude of fluctuations is comparable to that near the recirculation region. However, as time progresses, the fluctuations downstream of the recirculation region gradually diminish relative to those near the recirculation region. These variations clearly depict the gradual evolution of the fluctuation field throughout the transient process, approaching the modes of the post-transient flow. Therefore, tDMDpc is an effective tool for extracting coherent structures during the transient process.

We perform tDMDpc for Re values other than 100 to investigate the dependence of flow variation on Re . For $Re \approx 150$, the vortex street transitions to a secondary vortex in the post-transient flow (Taneda 1959; Jiang & Cheng 2019). In this case, the wake vortex is no longer composed solely of harmonics of f_1 . However, since the scope of this study focuses on the transient process from a steady flow, the secondary vortex falls outside the focus of this work. Therefore, this study addresses the transient process only for $Re \leq 100$, which is sufficiently smaller than 150.

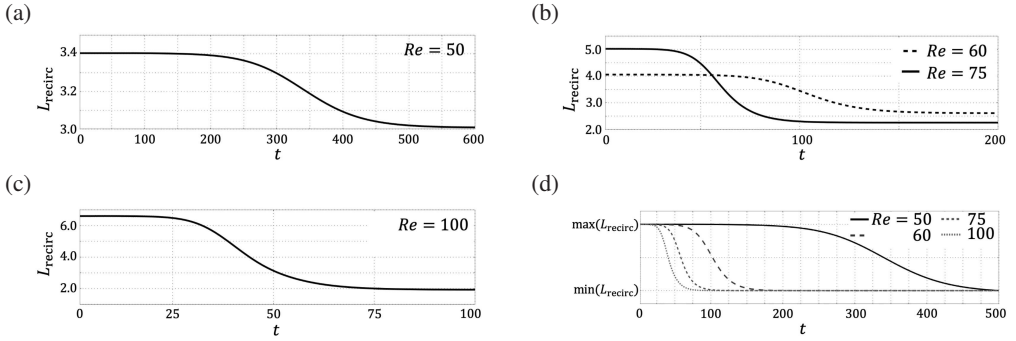


Figure 18: Time variation of L_{recirc} in the transient process: (a) $Re = 50$, (b) 60 and 75, (c) 100, and (d) $Re = 50, 60, 75, 100$, and 150, normalized by the maximum and minimum L_{recirc} .

For $Re = 50, 60$, and 75 , initial fields were prepared using the eigenmode from GSA with $j_{\text{max}} = 20$ for each Re , and time-series data for the transient process were obtained. From these transient data, we computed the flow field averaged over α as described in (2.17) for each Re . Figure 18 illustrates the temporal evolution of the recirculation region length, L_{recirc} , in the averaged flow field for $Re = 50, 60, 75$, and 100 . For all Re values, L_{recirc} decreases over time. After a sufficiently long growth, the recirculation region stabilizes at a constant length, although the time required to reach this steady state is longer for smaller Re values. Figure 18 (d) presents a normalized plot of L_{recirc} for the four Re cases, where the vertical axis is scaled by the maximum and minimum lengths of the respective recirculation regions. The temporal variation trends of L_{recirc} are remarkably similar across all Re cases.

We performed tDMDpc using time-series data of transient processes at four Re values and extracted time-varying modes along with their growth rates. A gradual variation in the mode distribution over time was observed for all four Re values; however, for simplicity, the mode distributions are omitted here. For a more quantitative analysis, Figure 19 shows the time variation of the growth rates of the f_1 -frequency mode at the four Re values. The growth rate gradually decreases over time and eventually reaches 0. This indicates that the perturbation field, which grows rapidly around the steady field, ultimately converges to a stable periodic flow. The trend in the time variation of the growth rates closely resembles the time variation of the recirculation region. This suggests a potential connection between the recirculation region and the growth of perturbation fields. Since the growth rate is directly linked to energy transfer, as derived from the global energy transfer equation, investigating energy transfer in transient processes could provide further insight into these potential relationships.

5.2. Energy transfer properties in transient process

To investigate the time variation of the energy at arbitrary times in the transient process, we computed the amplitudes of eigenmodes from tDMDpc. Figure 20 shows the time variation of amplitude $|a_{f_i}|$ at $Re = 50, 60, 75$, and 100 . The amplitude increases over time during the transient process and eventually converges to a stable constant. This is consistent with the convergence of the growth rate to 0 in tDMDpc. The growth process is monotonically increasing for $Re = 50$ and 60 , whereas a temporary maximum is observed at $Re = 75$ and 100 .

In the global energy transfer equation, the nonlinear triadic term related to $F_{f_i f_j f_k}$ is

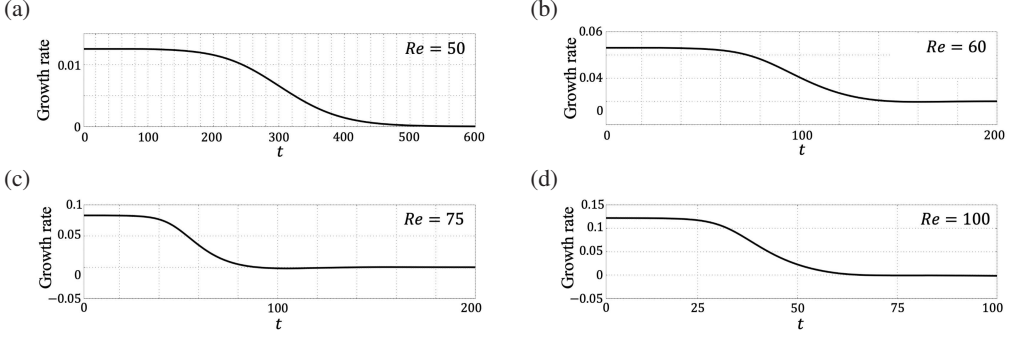


Figure 19: Time variation of growth rate in the transient process: (a) $Re = 50$, (b) 60, (c) 75, and (d) 100.

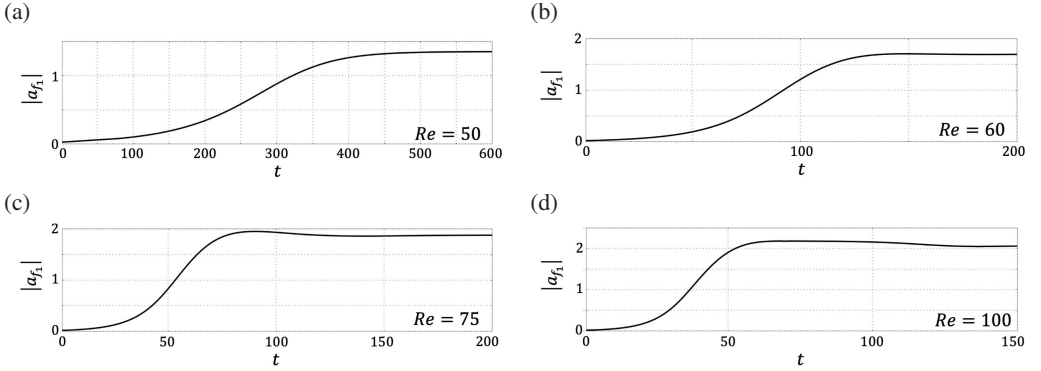


Figure 20: Time variation of mode amplitude $|a_{f_1}|$: (a) $Re = 50$, (b) 60, (c) 75, and (d) 100.

necessary to compute in the nonlinear case. Here, we define the nonlinear term as follows

$$\mathcal{N}_{f_k} = \sum_{i=\max(k-r, -r)}^{\min(k+r, r)} \text{Real}(a_{f_i} a_{f_{k-i}} a_{f_k}^* F_{f_i f_{k-i} f_k}) \quad (5.1)$$

In the ROM, the high-frequency modes are truncated, and the triadic term cannot be directly computed. Therefore, we evaluate the term of \mathcal{N}_{f_k} using the global energy transfer equation as follows

$$\mathcal{N}_{f_k}(t) = \frac{1}{2} \frac{d|a_{f_k}(t)|^2}{dt} - \text{Real}(G_{f_k f_k}) |a_{f_k}(t)|^2 \quad (5.2)$$

where the time variation of energy can be computed by forward differencing from the mode amplitude presented below

$$\frac{d|a_{f_1}(t)|^2}{dt} = \frac{|a_{f_1}(t + \Delta T)|^2 - |a_{f_1}(t)|^2}{\Delta T}. \quad (5.3)$$

Figure 21 shows the time variation of the time derivative of energy and $\text{Real}(G_{f_1 f_1}) |a_{f_1}|^2$ computed from the eigenmode of tDMDpc at $Re = 50, 60, 75$, and 100. At each of the four Re values, the time variation of energy is temporarily maximal during the transient process. After sufficient evolution, the time variation of energy becomes 0, but $\text{Real}(G_{f_1 f_1}) |a_{f_1}|^2$ converges to a positive value. These values differ due to the energy transfer of \mathcal{N}_{f_k} .

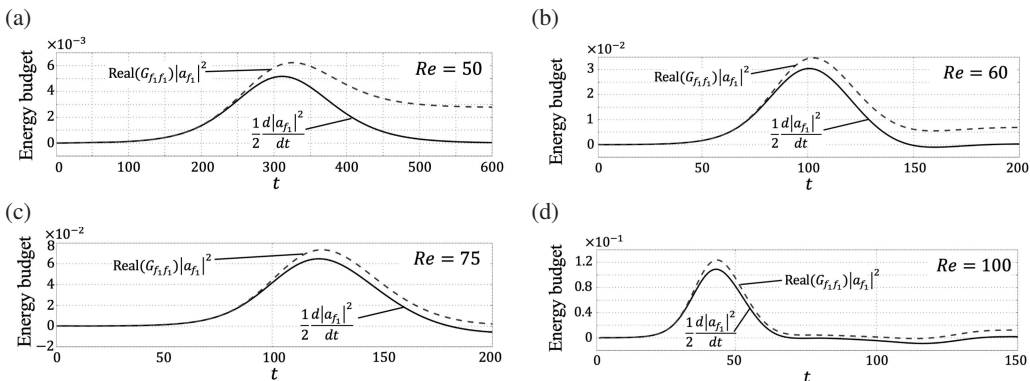


Figure 21: Time variation of kinetic energy for f_1 -frequency mode $d|a_{f_1}|^2/2dt$, and energy transfer derived from linear term $\text{Real}(G_{f_1, f_1})|a_{f_1}|^2$: (a) $Re = 50$, (b) 60, (c) 75, (d) 100. Difference of $d|a_{f_1}|^2/2dt$ and $\text{Real}(G_{f_1, f_1})|a_{f_1}|^2$ is equal to triadic energy transfer.

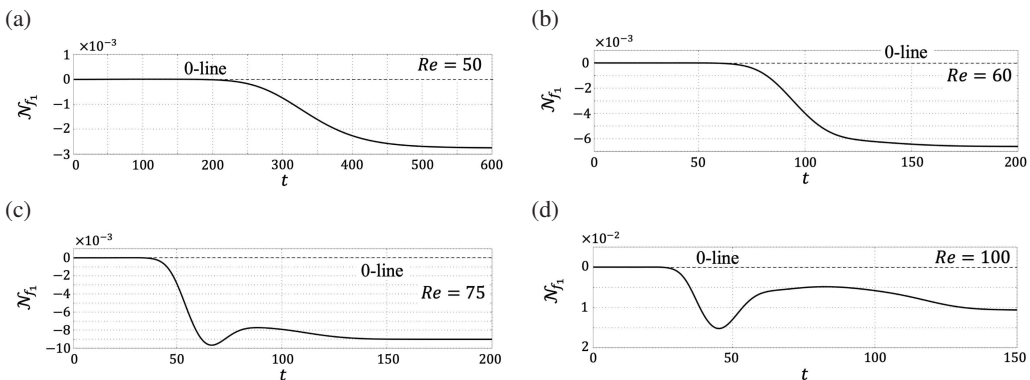


Figure 22: Time variation of difference between $d|a_{f_1}|^2/2dt$, and $\text{Real}(G_{f_1, f_1})|a_{f_1}|^2$ (triadic energy transfer): (a) $Re = 50$, (b) 60, (c) 75, and (d) 100. Triadic energy transfer decreases monotonically at $Re = 50$ and 60. Above $Re = 75$, it reaches a minimum value in a transient process and remains constant after increasing.

Figure 22 shows the time variation of \mathcal{N}_{f_1} , computed as the difference between $d|a_{f_1}|^2/2dt$ and $\text{Real}(G_{f_1, f_1})|a_{f_1}|^2$. The energy transfer remains negative across all times, indicating that energy is consistently transferred to higher-frequency modes. Since f_1 is the lowest frequency in the eigenvalue distribution of tDMDpc, \mathcal{N}_{f_1} represents energy transfer to higher-frequency modes. Thus, the negative value confirms a totally forward cascade process, where energy is transferred from f_1 to its harmonics.

Focusing on the time variation, for $Re = 50$ and 60, \mathcal{N}_{f_1} decreases monotonically throughout the transient process. In contrast, for $Re = 75$ and 100, \mathcal{N}_{f_1} reaches a temporary minimum before increasing and stabilizing in the steady state. This temporary fluctuation suggests a kind of nonlinearity. Therefore, these results indicate that nonlinearity becomes more pronounced as Re increases.

To investigate the variation of energy transfer in transient processes, we decompose $\text{Real}(G_{f_1, f_1})$ into three terms: \mathcal{D}_{f_1} , $\mathcal{T}_{\Delta \rightarrow f_1}$, and $\mathcal{T}_{f_1 \rightleftharpoons \Delta}$, following the energy transfer analysis around a steady field. These terms are computed from $\varphi_{f_1}(t)$ at each time step, and the corresponding values $\mathcal{D}_{f_1}|a_{f_1}|^2$, $\mathcal{T}_{\Delta \rightarrow f_1}|a_{f_1}|^2$, and $\mathcal{T}_{f_1 \rightleftharpoons \Delta}|a_{f_1}|^2$ are obtained using time-varying

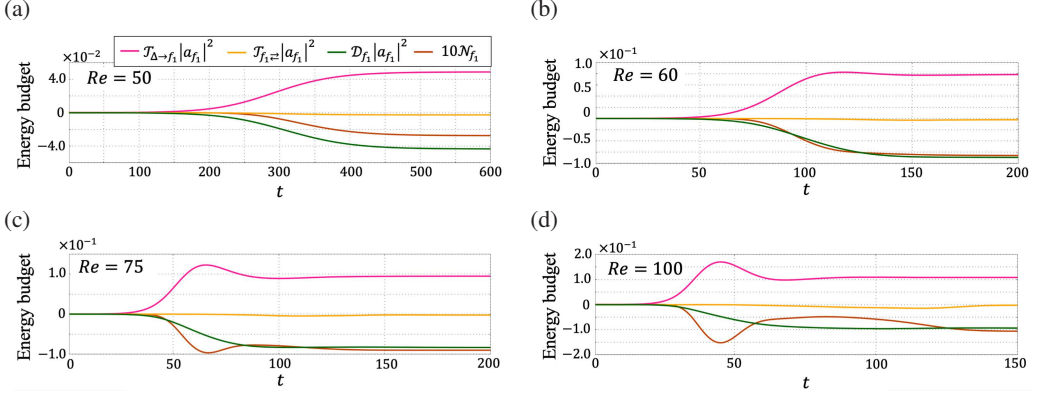


Figure 23: Time variation of four energy transfer term $\mathcal{D}_{f_1} |a_{f_1}|^2$, $\mathcal{T}_{\Delta \rightarrow f_1} |a_{f_1}|^2$, $\mathcal{T}_{f_1 \leftrightarrow} |a_{f_1}|^2$, and $10\mathcal{N}_{f_1}$: (a) $Re = 50$, (b) 60, (c) 75, and (d) 100.

$\mathcal{D}_{f_1}(t)$, $\mathcal{T}_{\Delta \rightarrow f_1}(t)$, $\mathcal{T}_{f_1 \leftrightarrow}(t)$, and $a_{f_1}(t)$. Figure 23 illustrates the time variation of the terms on the right-hand side of the global energy transfer equation (3.39): $\mathcal{D}_{f_1} |a_{f_1}|^2$, $\mathcal{T}_{\Delta \rightarrow f_1} |a_{f_1}|^2$, $\mathcal{T}_{f_1 \leftrightarrow} |a_{f_1}|^2$, and \mathcal{N}_{f_1} . Here, \mathcal{N}_{f_1} is plotted at 10 times its actual value to facilitate comparison with the other terms. Since $\mathcal{T}_{\Delta \rightarrow f_1} |a_{f_1}|^2$ is positive, while $\mathcal{T}_{f_1 \leftrightarrow} |a_{f_1}|^2$ and $\mathcal{D}_{f_1} |a_{f_1}|^2$ are negative, the energy transfer relationships observed in the steady field \mathbf{u}_Δ and the f_1 -frequency mode φ_{f_1} , characterized by a dynamical system linearized around the steady-state field, also hold in transient processes.

Focusing on the time variation of each term, the diffusion term decreases monotonically with time for all Re , indicating that diffusion effects become more significant as the f_1 -frequency component develops. Similarly, $\mathcal{T}_{f_1 \leftrightarrow} |a_{f_1}|^2$ remains slightly negative. As seen in the time variation of \mathcal{N}_{f_1} in figure 22 (also shown as the brown line in figure 23), all terms exhibit monotonic behavior at $Re = 50$. At $Re = 60$, $\mathcal{T}_{f_1 \leftrightarrow} |a_{f_1}|^2$ reaches a maximum before slightly decreasing to a steady state. Since this trend is absent in \mathcal{N}_{f_1} at $Re = 60$, this suggests that $Re = 60$ is close to the transition point where the monotonic development observed at $Re = 50$ shifts to the nonlinear development seen at $Re = 75$. For $Re = 75$ and 100, the decline after the peak of $\mathcal{T}_{\Delta \rightarrow f_1} |a_{f_1}|^2$ becomes more pronounced. Notably, the peak of $\mathcal{T}_{\Delta \rightarrow f_1} |a_{f_1}|^2$ nearly coincides with the minimum of \mathcal{N}_{f_1} . This suggests that as energy transfer from the steady field to the f_1 -frequency component increases, energy transfer to higher-frequency components also intensifies. That is, a hierarchical energy transfer structure can be inferred, where energy flows from the steady field into the f_1 -frequency component and subsequently cascades from the upper f_1 -frequency component to lower f_1 -harmonics components.

For a more quantitative comparison of the energy transfer with Re , normalizing the four terms $\mathcal{D}_{f_1} |a_{f_1}|^2$, $\mathcal{T}_{\Delta \rightarrow f_1} |a_{f_1}|^2$, $\mathcal{T}_{f_1 \leftrightarrow} |a_{f_1}|^2$, and \mathcal{N}_{f_1} for each Re , and each time is reasonable. The simplest normalization uses the sum of all terms; thus, it is $d|a_{f_1}|^2/2dt$ at each time. For instance, in the cases of $\mathcal{D}_{f_1} |a_{f_1}|^2$, as follows

$$\mathcal{D}_{f_1}(t) |a_{f_1}(t)|^2 \rightarrow \frac{\mathcal{D}_{f_1}(t) |a_{f_1}(t)|^2}{\frac{d|a_{f_1}(t)|^2}{2dt}}. \quad (5.4)$$

However, as shown in figure 21, $d|a_{f_1}|^2/2dt$ is not suitable for normalization because it temporarily becomes 0 during the transient process, leading to the divergence of normalized values. Therefore, we chose the $\mathcal{T}_{\Delta \rightarrow f_1} |a_{f_1}|^2$ for normalization, which is the major source of

energy. For instance, in the cases of $\mathcal{D}_{f_1}|a_{f_1}|^2$, as follows

$$\check{\mathcal{D}}_{f_1}(t) = \frac{\mathcal{D}_{f_1}(t)|a_{f_1}(t)|^2}{\mathcal{T}_{\Delta \rightarrow f_1}(t)|a_{f_1}(t)|^2}. \quad (5.5)$$

where $\check{\cdot}$ represents the normalized variables. In this manner, the damping amount of each term in the supply is obtained at an arbitrary time. In the steady state after sufficient time evolution,

$$-\check{\mathcal{D}}_{f_1}(t) - \check{\mathcal{T}}_{f_i \rightleftharpoons}(t) - \check{\mathcal{N}}_{f_1}(t) = 1, \quad (5.6)$$

due to $d|a_{f_1}|^2/2dt = 0$.

Figure 24 shows the time variation of $\check{\mathcal{D}}_{f_1}(t)$, $\check{\mathcal{T}}_{f_i \rightleftharpoons}(t)$, and $\check{\mathcal{N}}_{f_1}(t)$, normalized by $\mathcal{T}_{\Delta \rightarrow f_1}|a_{f_1}|^2$. For all Re , the diffusion term $\check{\mathcal{D}}_{f_1}(t)$ accounts for the largest portion of energy diffusion at all times. Comparing the time variation of $\check{\mathcal{D}}_{f_1}(t)$ across different Re provides insights into the Re -dependence of the transient process. Figure 24 (e) presents an overlay plot of the time evolution of the normalized $\check{\mathcal{D}}_{f_1}(t)$ for four different Re . In the steady state, 80–90% of the energy supplied by the \mathbf{u}_Δ is dissipated through $\check{\mathcal{D}}_{f_1}(t)$, and this characteristic is independent of Re .

Near the initial steady field at $t = 0$, the relative contribution of diffusion to the total energy budget decreases as Re increases. This suggests that the increase in energy transfer from the steady field to the f_1 -frequency mode at higher Re is more significant than any potential decrease in diffusion. This observation aligns with the Re -dependence of energy transfer around the steady field shown in figure 9. The time evolution of energy diffusion for $Re = 75$ and 100 exhibits a distinct behavior compared to lower Re cases. Specifically, unlike other Re values, the diffusion rate temporarily increases before stabilizing. This indicates that, during the transient process, a substantial portion of the energy was dissipated within a short period, facilitating the convergence of the flow field to the steady state at $Re = 75$ and 100. Conversely, for $Re = 50$ and 60, the flow field stabilizes gradually through a continuous diffusion of the energy supplied from \mathbf{u}_Δ . This contrast in transient behavior highlights the nonlinear nature of flow evolution, as the energy diffusion mechanisms vary depending on the Re regime.

The ratio of $\mathcal{T}_{\Delta \rightarrow f_i}|a_{f_i}|^2$ to $\mathcal{D}_{f_1}|a_{f_1}|^2$ depends on the Re , largely due to the variation of energy transfer depend on Re . This motivates us to investigate the energy transfer fields $\mathcal{T}_{\Delta \rightarrow f_i}|a_{f_i}|^2$. Figure 25 shows the time-variation of energy transfer fields $\mathcal{T}_{\Delta \rightarrow f_i}|a_{f_i}|^2$ at $Re = 50, 60$, and 100. The 0-line of \mathbf{u}_Δ at the same t is plotted by the white line. The positive energy transfer region moves to the near cylinders with time variation. At $t = 80$ with a $Re = 100$, particularly strong energy transfer is observed near the recirculation region of the cylinder wake and on the $y = 0$. This distribution of energy transfer fields is very similar to transfer fields at post-transient flow fields at $Re = 100$ reported in (Yeung *et al.* 2024). The distributions at $t = 100$ and $t = 30$ for $Re = 100$ are quite different, but we can see how they gradually change continuously with time evolution. Continuous changes can be seen even at $Re = 50$ and 60.

We focus on the relationship between the location of the recirculation region indicated by the white line and the energy transfer distribution. For qualitatively at $Re = 100$, the 0-line and energy transfer distributions maintain almost the same x position at all times. Conversely, for $t = 300$ at $Re = 70$ and $Re = 50$, the transfer distribution exists at a distance from the 0 line. It is possible that the difference in the development process between $Re = 50$ and 100 (see figure 24 and figure 22) is due to this difference in the transfer fields.

We quantitatively investigate the relationship between the energy transfer field and the recirculation region. Similar to the energy transfer analysis around a steady field, the location

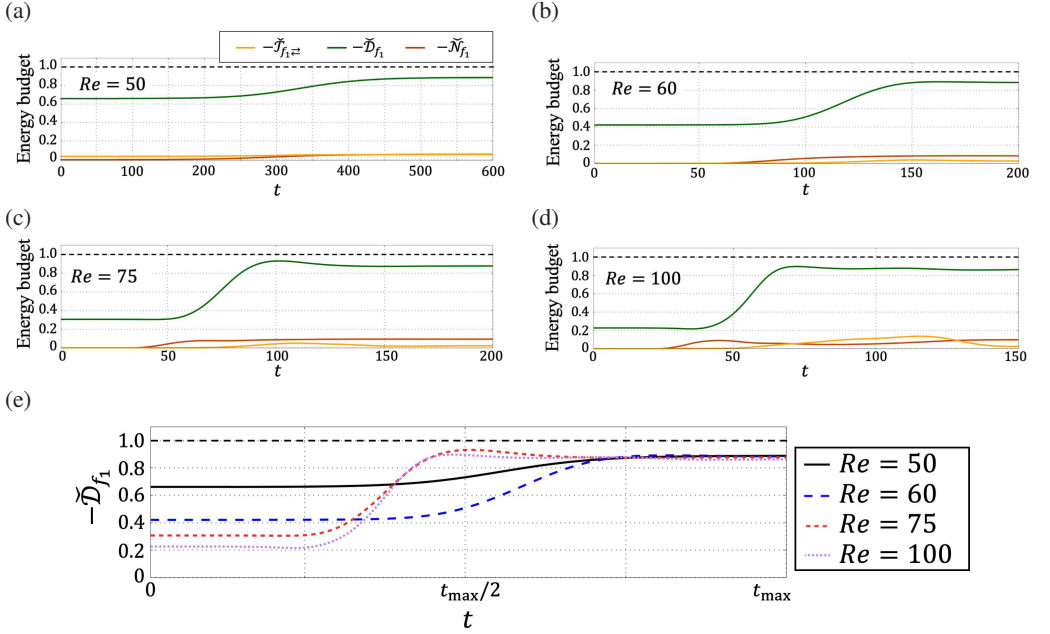


Figure 24: Time variation of energy transfer term $\mathcal{D}_{f_1} |a_{f_1}|^2$, $\mathcal{T}_{f_i \rightleftharpoons} |a_{f_1}|^2$, and \mathcal{N}_{f_1} , normalized by $\mathcal{T}_{\Delta \rightarrow f_i} |a_{f_1}|^2$: (a) $Re = 50$, (b) $Re = 60$, (c) $Re = 75$, (d) $Re = 100$, (e) overlay plot of $\mathcal{D}_{f_1} |a_{f_1}|^2$ with different Re . The t_{\max} on the horizontal axis in (e) is the maximum value of the horizontal axis in (a), (b), (c), and (d)

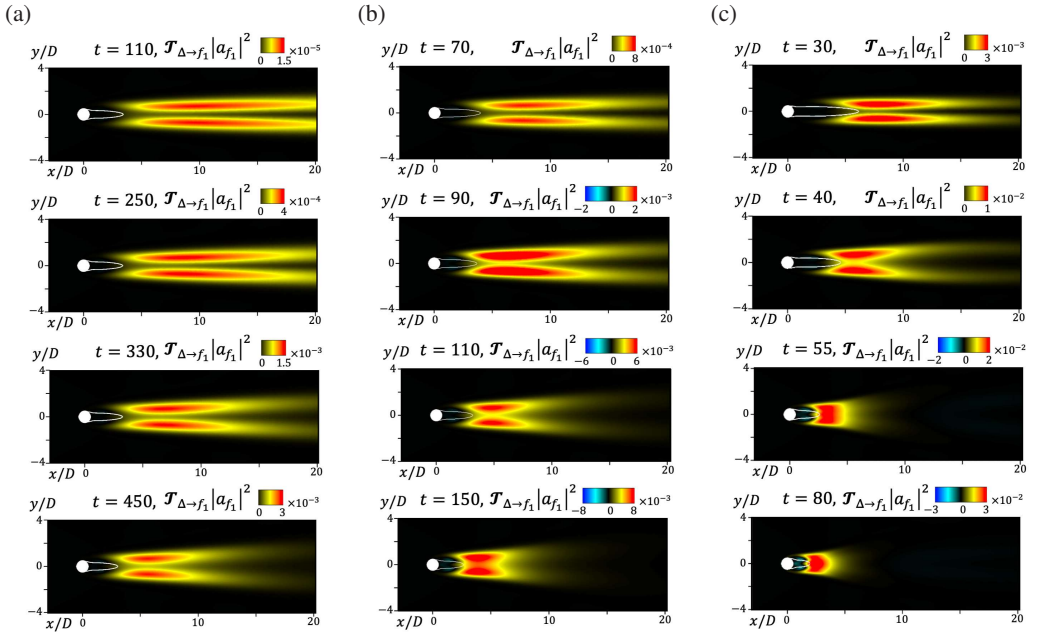


Figure 25: Spatial distribution of transfer fields $\mathcal{T}_{\Delta \rightarrow f_i} |a_{f_i}|^2$ obtained from eigenmodes of tDMDpc (a) $Re = 50$, (b) 60 , and (c) 100 .

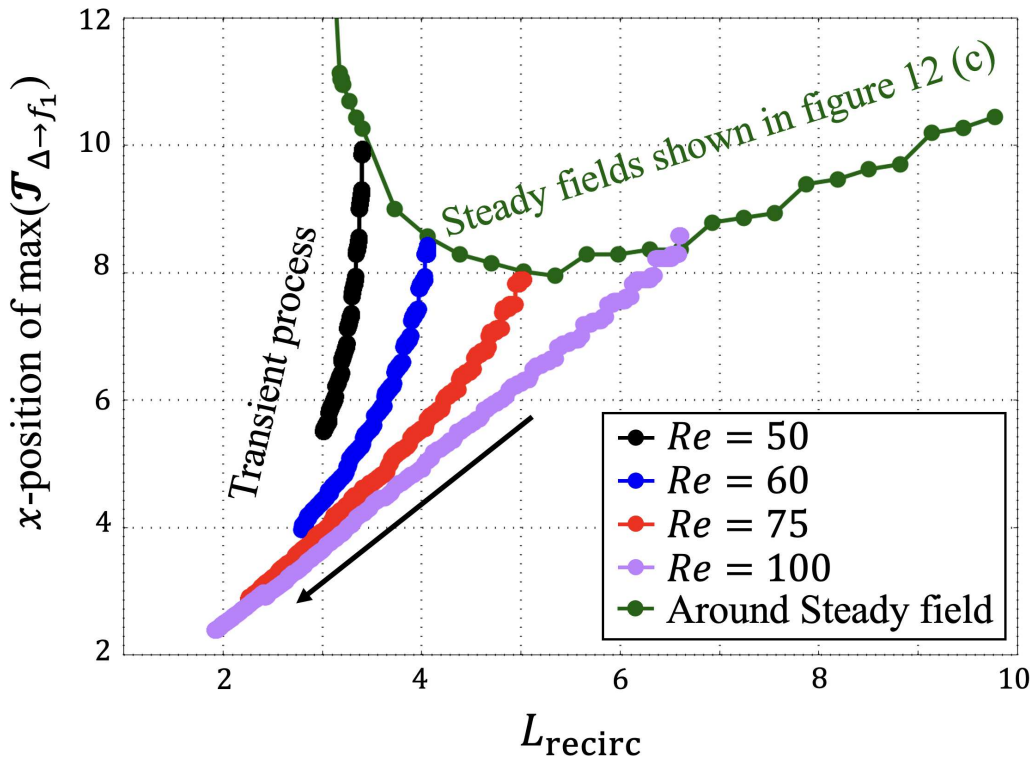


Figure 26: The x -position of the maximum value of the transfer fields $\mathcal{T}_{\Delta \rightarrow f_i}$ for various Re and transient process.

of the primary energy transfer is characterized by the maximum value x -position of $\mathcal{T}_{\Delta \rightarrow f_i}$. Figure 26 shows the relationship between the x -position at $\max(\mathcal{T}_{\Delta \rightarrow f_i})$ and the x -coordinate position of the 0-line of the recirculation region L_{recirc} . The green lines are the results of energy transfer analysis around the steady flow for various Re cases shown in figure 12 (c). At a $Re = 100$, the energy transfer position follows the recirculation region linearly. Even in the transient process at a $Re = 75$, the gradually approaches to a linear line at $Re = 100$. At $Re = 50$, transient development ends before reaching the linear relationship line, as in $Re = 100$.

With the qualitative interpretation of the transfer fields, when L_{recirc} and $\max(\mathcal{T}_{\Delta \rightarrow f_i})$ are linearly related, the positions of the energy transfer and recirculation regions are almost the same. From the relation between L_{recirc} and $\max(\mathcal{T}_{\Delta \rightarrow f_i})$ with $Re = 50, 60$, and 75 the location of the transfer field and the location of the recirculation region become closer as the flow field develops. In summary, the location of energy transfers can be divided into two cases where they are concentrated on the recirculation region and they occur behind the recirculation region. With the result of the relationship between L_{recirc} and $\max(\mathcal{T}_{\Delta \rightarrow f_i})$ around the base flow, the former case suggests significant energy transfer, which accelerates the transient process.

6. Conclusion

This paper presents an energy transfer and budget analysis method for flow fields with growing or decaying modes. Furthermore, our approach extends to nonlinear development

scenarios. The energy transfer analysis is achieved using a projection-based ROM for operator eigenmodes obtained from GSA and DMD. The projected governing equations are organized using the bi-orthogonality between the eigenmodes of the operators and their adjoint modes. The equation is further simplified by considering the interaction of frequencies in a triadic relationship based on the frequencies of the operator eigenmodes. Based on the simplified equations, we derived the global energy transfer equations for the entire flow field at the frequencies of interest. The global energy transfer equations were developed into a simplified form when linearized around a steady field and into an advanced form when accounting for the time-varying operators and modes.

The transfer analysis results using GSA eigenmodes around a steady flow show that the growth rate obtained from GSA is expressed by the sum of energy transfer from the steady flow to the eigenmode, self-decay of the eigenmodes, and viscous diffusion. This indicates that the growth or decay of eigenmodes is governed by their energy budget. For the flow around a cylinder, the only source of eigenmode energy is the steady flow, and this supply is nearly nonexistent for Re values smaller than the bifurcation point. The decrease in the growth rate at Re lower than the bifurcation point is caused by the self-decay of the eigenmode. The spatial distributions causing these transfers and diffusion were computed from the eigenmodes and the steady field inspired by other modal energy analysis methods. When the Reynolds number is more significant than 80, there is a roughly linear relationship between the length of the recirculation region and the location of the maximum transfer distribution.

The energy transfer and budget analysis were extended to the transient development process by considering the time variation of eigenmodes due to time-varying operators. To extract time-varying operator eigenmodes, we introduced tDMDpc, which regulates the initial phase and applies DMD to data obtained from multiple numerical simulation cases. Using tDMDpc for two-dimensional flow around a cylinder, we obtained time-varying eigenmodes that grow from a steady field to a periodic unsteady scenario. The base flow is obtained by averaging the numerical results across different initial conditions. For flow around a cylinder, the recirculation region of the wake becomes smaller as the unstable eigenmode grows.

Using the time-varying eigenmodes obtained by tDMDpc, we computed the energy budget for the global energy transfer equation. This analysis specifically applies to the operator's time-varying eigenmodes rather than being restricted to modes from tDMDpc extraction. In the flow around a cylinder, energy transfer from the base flow to the lowest-frequency eigenmode drives transient development. Simultaneously, nonlinear interactions induce an energy cascade into higher-frequency modes, which peaks alongside the energy transfer to the lowest-frequency eigenmode.

To compare the energy budgets at different Re , we propose a method for normalizing by the amount of energy transferred from the steady flow to the low-frequency eigenmodes. Throughout any transient process, 80–90% of the energy transferred from the base flow is ultimately dissipated via viscous diffusion in the stable periodic flow. With this normalization, when a stable periodic flow is reached after a transient process, two types of cases emerge: one where the eigenmode stabilizes after a temporary increase in the viscous effect and the other where the eigenmode stabilizes after a gradual increase in the diffusion effect. These differences depend on the magnitude of energy transferred from the base flow to the eigenmodes. The spatial distribution of transfer fields in the transient process indicates that a substantial amount of energy transfer from the base flow is concentrated around the recirculation region. Since this energy transfer field varies throughout the transient process, it serves as a powerful tool for observing the time-varying energy transfer distribution and discovering new flow physics.

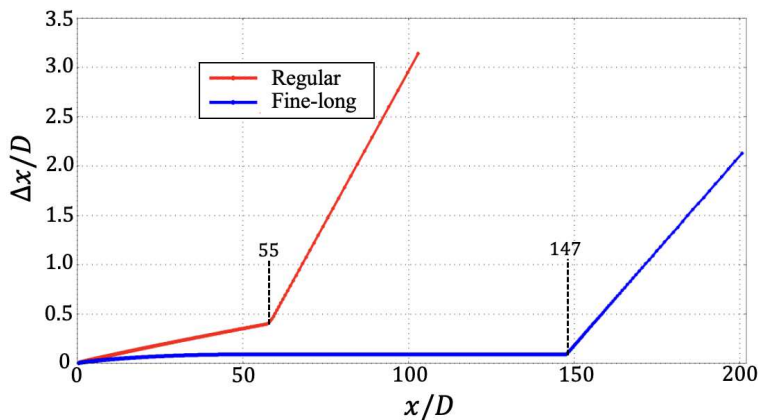


Figure 27: Cell width for regular and very fine-long grid.

Appendix A. Grid convergence

The computational grid used in this study is validated based on the parameter dependence check. Regular grids and fine-long grids were prepared to test the effect on numerical results of the grid width and the far-field boundary size. Figure 27 shows the grid widths of the grids located on the x -axis in the two computational grids. The regular and fine-long grids accelerate the expansion of the grid width when the radius is greater than 55 and 147, respectively. The expansion ratio of the neighboring cell is less than or equal to 1.1. The number of cells for fine-long grids is 580 in the wall-parallel direction and 2260 in the wall-normal direction.

Numerical simulations were performed for a $Re = 150$ using two computational grids. CFL number is set at less than or equal to 1.0 based on the validation of our previous work (Nakamura *et al.* 2024, Kobe, Japan). For quantitative comparison, the time-averaged velocity field $\bar{\mathbf{u}}(\mathbf{x})$ and the time-averaged kinetic energy $\overline{\mathbf{u}\mathbf{u}}(\mathbf{x})$ and $\overline{\mathbf{v}\mathbf{v}}(\mathbf{x})$ are computed as

$$\bar{\mathbf{u}}(\mathbf{x}) = \frac{1}{T} \int \mathbf{u}(t, \mathbf{x}) dt, \quad (\text{A } 1)$$

$$\overline{\mathbf{u}\mathbf{u}}(\mathbf{x}) = \frac{1}{T} \int \tilde{\mathbf{u}}(t, \mathbf{x}) \tilde{\mathbf{u}}(t, \mathbf{x}) dt = \frac{1}{T} \int \mathbf{u}(t, \mathbf{x}) \mathbf{u}(t, \mathbf{x}) dt - \bar{\mathbf{u}}(\mathbf{x}) \bar{\mathbf{u}}(\mathbf{x}), \quad (\text{A } 2)$$

$$\overline{\mathbf{v}\mathbf{v}}(\mathbf{x}) = \frac{1}{T} \int \tilde{\mathbf{v}}(t, \mathbf{x}) \tilde{\mathbf{v}}(t, \mathbf{x}) dt = \frac{1}{T} \int \mathbf{v}(t, \mathbf{x}) \mathbf{v}(t, \mathbf{x}) dt - \bar{\mathbf{v}}(\mathbf{x}) \bar{\mathbf{v}}(\mathbf{x}). \quad (\text{A } 3)$$

based on Asada (2014). Here, T is set to 300, which is long enough since the primary dimensionless period of the vortex shedding is about 5.

Figure 28 shows the distribution of $\bar{\mathbf{u}}(\mathbf{x})$, $\overline{\mathbf{u}\mathbf{u}}$, and $\overline{\mathbf{v}\mathbf{v}}$ in the x and y directions. The distributions in the x direction for $x/D < 20$ shown in figure 28 (a) are in better agreement for the regular and fine-long grids. The range of the x -direction was chosen because most of the energy transfer occurs at $x/D < 20$. Since the deviation of the kinetic energy distribution is relatively larger than that of the average field, the kinetic energy distribution is focused in the y direction distribution shown in figure 28 (b). The x -section coordinates position was chosen to be $x/D = 2.23$ and 20. $x/D = 2.23$ is selected since the peak value position of $\overline{\mathbf{v}\mathbf{v}}$ on the x -axis. The y -axis distribution of kinetic energy in the streamwise direction at $x/D = 2.23$ and 20 is in close agreement with the regular and fine-long grids. Therefore, the resolution of numerical results with the regular grid is enough for this work.

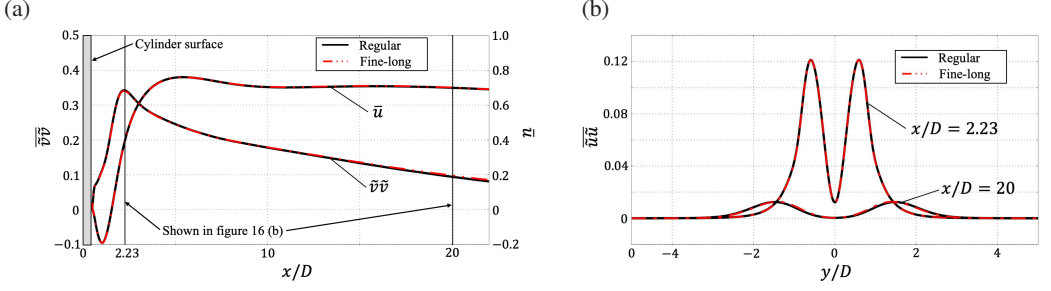


Figure 28: Comparison of the regular grid and fine-long grid with the average value of kinetic energy distribution $\overline{u\bar{u}}$, $\overline{v\bar{v}}$, and streamwise velocity fields \bar{u} , (a) distribution on the x -axis of $\overline{v\bar{v}}$ and \bar{u} , (b) y -direction distribution of $\overline{u\bar{u}}$ and \bar{u} at $x/D = 20, 2.23$. $x/D = 2.23$ is the peak value position of $\overline{v\bar{v}}$.

Appendix B. Validation of time stepping GSA and parameter dependance

We check the validity of time-stepping GSA and the resulting eigenvalues and eigenmodes. The validity is divided into two parts: checking the dependence of parameters in time-stepping GSA and checking Re dependence.

B.1. Time-stepping GSA parameter dependance

Time-stepping GSA has two parameters, ΔT and ϵ_0 . In this paper, ΔT is fixed at 0.1, and the parameter dependence is tested by varying the magnitude of ϵ_0 .

For investigate the effect of ϵ_0 , time-stepping GSA was performed on $\epsilon_0 = 10^{-6}, 10^{-3}$, and 10^0 at $Re = 100$. Figure 29 shows the initial disturbance at $\epsilon_0 = 10^{-3}$. Following Ranjan *et al.* (2020), the initial disturbance was generated only near the cylinder. Figure 30 shows instantaneous streamwise components of velocity and perturbation. For $\epsilon_0 = 10^{-6}$ and 10^{-3} , the distribution of streamwise component is an almost steady field. This is because the amount of perturbation, whose absolute value is determined by ϵ_0 , is smaller than that of the steady field. In contrast, when $\epsilon_0 = 10^0$, the magnitude of the perturbation is larger than the magnitude of the steady field, and the flow distribution is unphysical. In addition, for small values of $\epsilon_0 = 10^{-6}$, the perturbation distribution is symmetric to $y = 0$, and no asymmetric Karman vortex is formed. This is due to the suppression of fluctuations by small ϵ_0 during the development process of disturbance, and disturbance does not grow to the formulation of the Karman vortex.

To quantitatively evaluate the effect of ϵ_0 , growth rates were computed for several ϵ_0 and Re cases. Figure 31 shows the variation of growth rate with respect to ϵ_0 at $Re = 35, 60$, and 100. The growth rate is constant for all Re cases when ϵ_0 is sufficiently large. However, in general, time-stepping GSA must be performed within a range where ϵ_0 is small; otherwise, the flow fields grow beyond the linear growth region. Therefore, this study uses $\epsilon_0 = 10^{-3}$ in all cases.

B.2. Validation for Reynolds number dependance

Since the comparison with previous studies on the Reynolds number dependence is mentioned in figure 7, here we compare our results with those of ordinary CFD results. However, due to the difficulty of comparing the results of CFD and GSA under conditions of rapidly developing conditions at a relatively high Re , the results are compared near the bifurcation point. The growth rates and frequencies near the bifurcation point are shown in table 1. Between $Re = 46.8$ and 46.9, the growth rate changes from negative to positive. Since the

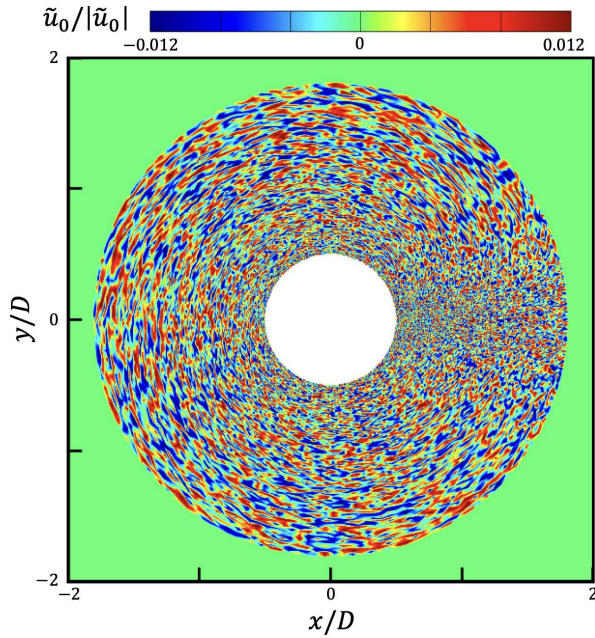


Figure 29: Initial disturbance for streamwise-velocity component at time-stepping GSA.

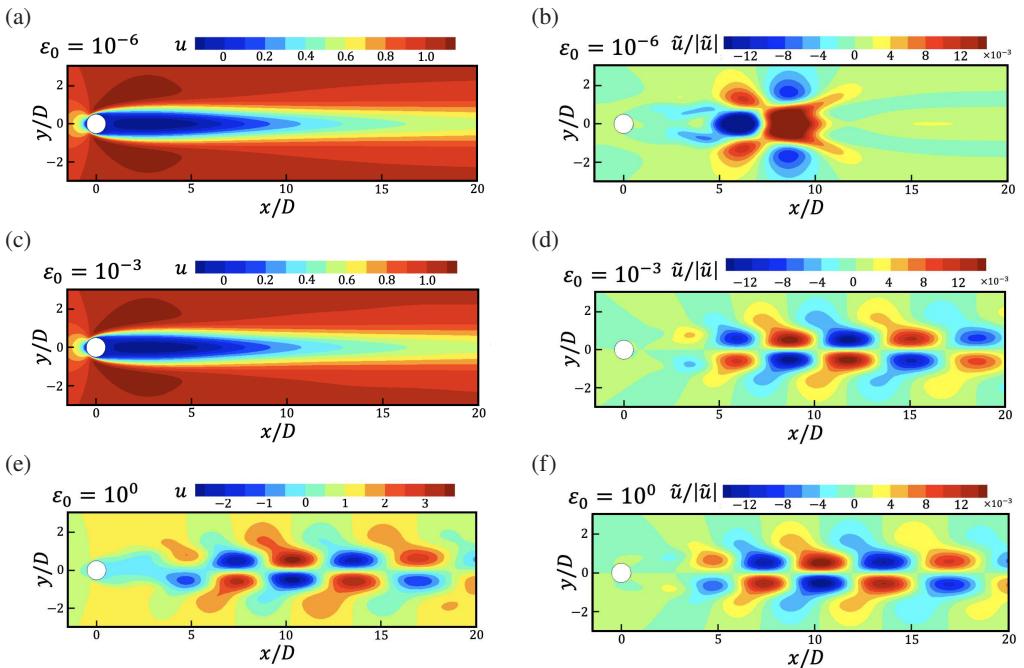


Figure 30: Instantaneous streamwise component of velocity and perturbation at $Re = 100$ and $t = 50$ in the time-stepping approach; (a) velocity with ($\epsilon_0 = 10^{-6}$), (b) perturbation with ($\epsilon_0 = 10^{-6}$), (c) velocity with ($\epsilon_0 = 10^{-3}$), (d) perturbation with ($\epsilon_0 = 10^{-3}$), (e) velocity with ($\epsilon_0 = 10^0$), and (f) perturbation with ($\epsilon_0 = 10^0$).

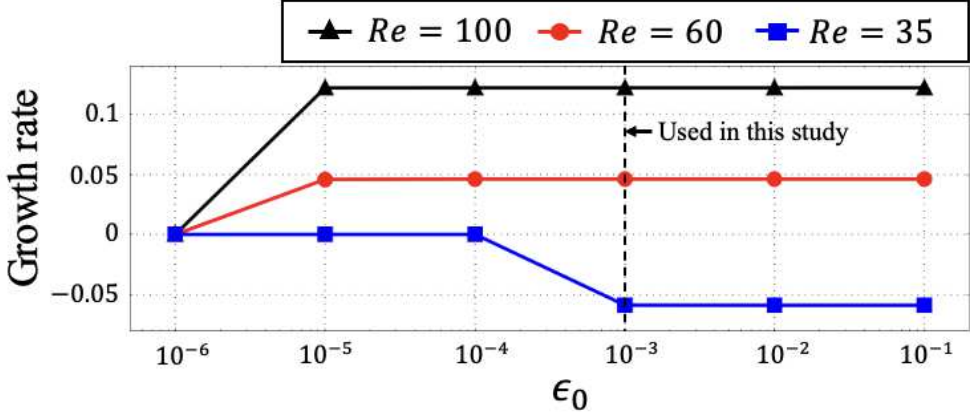


Figure 31: Variation of growth rate for various ϵ_0 with $Re = 35, 60, 100$.

Re	Growth rate	Frequency
45.0	-7.79034×10^{-3}	0.115833
46.5	-1.37338×10^{-3}	0.116221
46.6	-9.54785×10^{-4}	0.116246
46.7	-5.37557×10^{-4}	0.116269
46.8	-1.21642×10^{-4}	0.116294
46.9	2.93599×10^{-4}	0.116319
47.0	7.07521×10^{-4}	0.116343
50.0	1.26154×10^{-2}	0.116973

Table 1: Growth rate and frequency near the bifurcation point.

absolute value of the growth rate is minimum at $Re = 46.8$, the bifurcation point is roughly 46.8.

The development of flow fields with $Re = 46.8$ and 46.9 are computed by CFD without explicitly including disturbances. Figure 32 shows the residuals of the velocity vector in the flow field obtained by CFD. Here, the velocity residual is computed by

$$(\text{Velocity residual}) = \frac{1}{N\Delta T} \sum_{i=1}^N |\mathbf{u}(\mathbf{x}_i, t + \Delta T) - \mathbf{u}(\mathbf{x}_i, t)|, \quad (\text{B } 1)$$

where \mathbf{x}_i represents i th grid points. No increase in residuals is confirmed for $Re = 46.8$, but for $Re = 46.9$, the residuals gradually increase. An increase in residuals implies a sign of non-stationarity. Hence, the bifurcation point in the CFD obtained by the GSA is in close agreement. To compare the frequency of growing modes from CFD, DMD is applied to $t = 1000-2000$ at $Re = 46.9$. The obtained frequency is 0.116305, and growth rate is 4.87011×10^{-4} . Therefore, the time-stepping GSA presents the linear growing eigenmodes in the CFD.

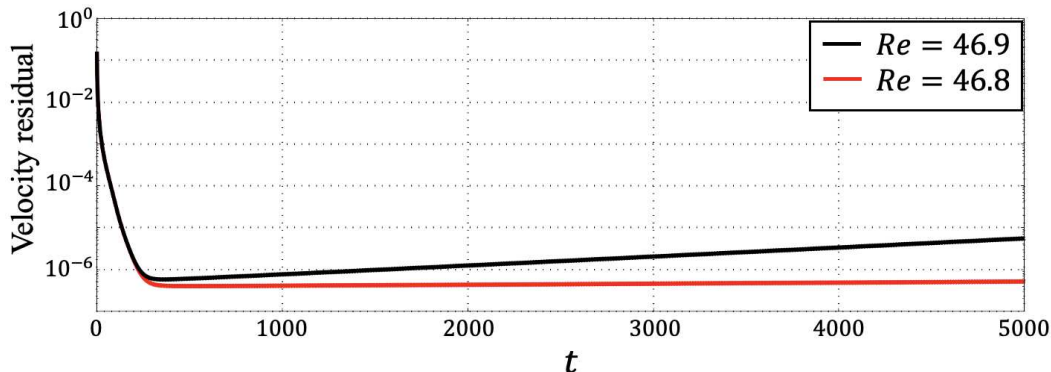


Figure 32: Velocity residuals for the numerical simulation at $Re = 46.8$ and 46.9 . In the present simulation, critical Re is determined to be 46.8 , as the velocity residual remains at a constant order, which is consistent with the GSA result.

Appendix C. Convergence study of tDMDpc

For tDMDpc, the number of conditions j_{\max} is the number of snapshots in the eigenmode extraction using DMD. The validity of eigenmode extraction for time-dependent operators can be evaluated by the fact that the eigenmodes remain constant when the number of snapshots is sufficiently large. First, we check that the average field over α does not change as increasing j_{\max} .

Figure 33 shows the time variation of the average field over α at $y/D = 0$ for $j_{\max} = 20$ and 100 . The average fields during the development process are completely consistent between 20 and 100 cases, and the average field for $j_{\max} = 20$ cases is well converged. To quantitatively evaluate whether the flow field reaches a periodic state after the transient development, the mean field of the fully developed periodic flow is shown by the blue dotted line. Note that the fully developed periodic flow refers to the flow fields at $t \geq 2000$, averaged over $t = 2000$ – 2300 , and not averaged over α . Moreover, after a sufficient time evolution, the average field over α exhibits a reasonable distribution, as it coincides with the mean-field represented by the blue dotted line.

We check the convergence of the eigenmodes of the non-0 frequencies of the time-varying operator. Turning to the mode extraction process in the DMD, the eigenmodes are computed by projecting the eigenmodes of the low-dimensional operator \tilde{A} by U_r^T . Since U_r is determined by the SVD of the dataset, the convergence of the matrix projected by U_r is confirmed by the singular values. Then, in a form independent of the number of snapshots, we define

$$\gamma_k = \frac{\sigma_k^2}{(M-1)} \quad (\text{C } 1)$$

where σ_k is the singular value of matrix X , thus, k th diagonal elements of S_r in equation (2.10). Here, γ_k equals the eigenvalue of variance-covariance matrix $XX^T/\sqrt{M-1}$ and POD eigenvalue. The convergence of γ_k with respect to snapshot number means the convergence of the major features of the snapshots that make up the matrix X and ensures a sufficient number of snapshots. This also suggests the DMD modes computed using the SVD results for X converge.

Figure 34 shows the time variation of γ_k for $j_{\max} = 20$ and 100 cases. The γ_k of DMD applied to the fully developed periodic flow is shown by the blue dotted line. Since singular values appear in pairs— $k = 2$ and 3 , $k = 4$ and 5 , \dots —the one with the larger is plotted in the

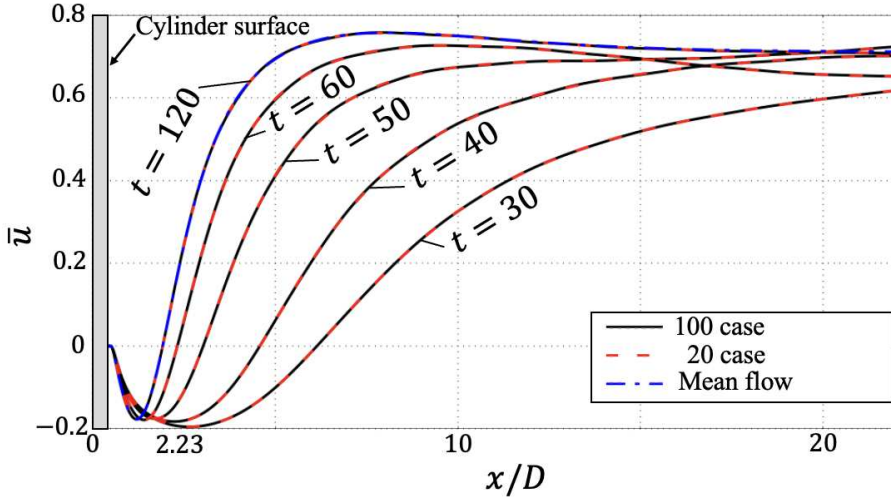


Figure 33: Average-fields of phase-controlled transient flow at $Re = 100$. Flow fields are averaged over 20 and 100 cases at $t = 30, 40, 50, 60, 80,$ and 120 . The blue dash-dot line shows the mean fields of the post-transient flow field, which is obtained from time-averaging of fully developed periodic flow fields.

figure. $k = 1$ corresponds to a mean field with no pair γ_k and, as shown in figure 33, has the same value at $j_{\max} = 20$ and 100 . The time variation of the value of γ_1 appears to be almost negligible because the energy of the far main flow is very large with respect to the transient variation for the cylinder backward. $k = 2$ corresponds to the most dominant eigenmode and is well converged at all times. For $k \geq 4$, in the early stage of development, γ_k value is very small and is considered to be affected by the errors in the numerical calculation of SVD. In the early stage, the spatial structure corresponding to $k \geq 4$ is too small or does not exist because the mode corresponding to $k \geq 4$ is not added to the disturbance at $t = 0$. However, after sufficient development, $j_{\max} = 20$ and 100 are close agreement. Therefore, $j_{\max} = 20$ is large enough for capturing the eigenmode of the time-varying operator.

Acknowledgements. We thank Prof. Oliver T. Schmidt for pointing to the convective instability. We gratefully acknowledge Dr. Yasuhito Okano for providing valuable knowledge about GSA. We thank Yuta Iwatani for the valuable discussions on nonlinear interactions and resolvent analysis and for pointing out the bi-orthogonality of the DMD mode.

Funding. The numerical simulations were performed on the supercomputer systems “AFI-NITY” and “AFI-NITY II” at the Advanced Fluid Information Research Center, Institute of Fluid Science, Tohoku University, and JAXA Supercomputer System Generation 3 (JSS3). This study was partially supported by a Sasakawa Scientific Research Grant from the Japan Science Society. This study was partially supported by JST SPRING, Grant Number JPMJSP2114, Japan.

Declaration of interests. The authors report no conflict of interest.

Author ORCIDs.

Y. Nakamura, <https://orcid.org/0009-0008-4118-1078>;

S. Sato, <https://orcid.org/0000-0002-9979-0051>;

N. Ohnishi, <https://orcid.org/0000-0001-5895-0381>

REFERENCES

AITZHAN, A., NOURI, A. G., GIVI, P. & BABAEI, H. 2025 Reduced order modeling of turbulent reacting flows on low-rank matrix manifolds. *Journal of Computational Physics* **521**, 113549.

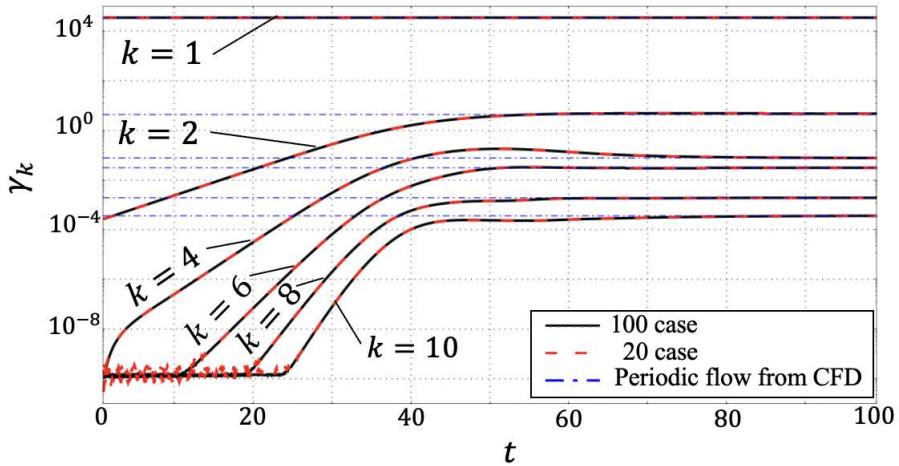


Figure 34: Square quantities of the singular value obtained from the SVD for matrix X in the DMD algorithm. All singular values were normalized by snapshot number, indicated in (C1). The blue dash-dot line is the γ_k computed from fully developed periodic flow fields.

- AKHTAR, I. 2008 Parallel simulation, reduced-order modeling, and feedback control of vortex shedding using fluidic actuators. PhD thesis, Virginia Polytechnic Institute and State University.
- AMIRI-MARGAVI, A. & BABAEI, H. 2024 Time-dependent low-rank input–output operator for forced linearized dynamics with unsteady base flows. *Journal of Fluid Mechanics* **1001**.
- ASADA, K. 2014 Computational analysis of flow fields induced by a DBD plasma actuator toward separated-flow control. Master’s thesis, University of Tokyo.
- BALLOUZ, E., DAWSON, S. T. M. & BAE, H. J. 2024 Transient growth of wavelet-based resolvent modes in the buffer layer of wall-bounded turbulence. In *Journal of Physics: Conference Series*, , vol. 2753, p. 012002. IOP Publishing.
- BARKLEY, D. 2006 Linear analysis of the cylinder wake mean flow. *Europhysics Letters* **75** (5), 750.
- BERKOOZ, G., HOLMES, P. & LUMLEY, J. L. 1993 The proper orthogonal decomposition in the analysis of turbulent flows. *Annual review of fluid mechanics* **25** (1), 539–575.
- BISWAS, N. & BUXTON, O. R.H. 2024 Energy exchanges between coherent modes in the near wake of a wind turbine model at different tip speed ratios. *Journal of Fluid Mechanics* **996**.
- DENG, N., NOACK, B. R., MORZYŃSKI, M. & PASTUR, L. R. 2019 Low-order model for successive bifurcations of the fluidic pinball. *Journal of Fluid Mechanics* **884**.
- FORNBERG, B. 1980 A numerical study of steady viscous flow past a circular cylinder. *Journal of Fluid Mechanics* **98** (4), 819–855.
- FREEMAN, B. R. S., MARTINUZZI, R. J. & HEMMATI, A. 2023 Exploring the influence of span-wise boundary conditions on the wake of a thin flat plate using Fourier-averaged Navier–Stokes equations. *International Journal of Heat and Fluid Flow* **103**, 109176.
- FREEMAN, B. R. S., MARTINUZZI, R. J. & HEMMATI, A. 2024 Momentum analysis of complex time-periodic flows. *Journal of Fluid Mechanics* **979**, A50.
- FUKAMI, K. 2024 *Data-Driven Modeling and Control of Extreme Aerodynamic Flows: Super Resolution, Manifold Identification, and Phase-Amplitude Reduction*. University of California, Los Angeles.
- GIANNETTI, F. & LUCHINI, P. 2007 Structural sensitivity of the first instability of the cylinder wake. *Journal of Fluid Mechanics* **581**, 167–197.
- GOUPILLAUD, P., GROSSMANN, A. & MORLET, J. 1984 Cycle-octave and related transforms in seismic signal analysis. *Geoexploration* **23** (1), 85–102.
- GUAN, W., DONG, L., ZHANG, A. & CAI, Y. 2024 Output-only modal identification with recursive dynamic mode decomposition for time-varying systems. *Measurement* **224**, 113852.
- HERRMANN, B., BADDOO, P. J., SEMAAN, R., BRUNTON, S. L. & MCKEON, B. J. 2021 Data-driven resolvent analysis. *Journal of Fluid Mechanics* **918**.
- HOLMES, P. 2012 *Turbulence, coherent structures, dynamical systems and symmetry*. Cambridge university press.

- IWATANI, Y., ASADA, H., YEH, C.-A., TAIRA, K. & KAWAI, S. 2023 Identifying the self-sustaining mechanisms of transonic airfoil buffet with resolvent analysis. *AIAA Journal* **61** (6), 2400–2411.
- JIANG, H. & CHENG, L. 2017 Strouhal–Reynolds number relationship for flow past a circular cylinder. *Journal of Fluid Mechanics* **832**, 170–188.
- JIANG, H. & CHENG, L. 2019 Transition to the secondary vortex street in the wake of a circular cylinder. *Journal of Fluid Mechanics* **867**, 691–722.
- KAJISHIMA, T. & TAIRA, K. 2017 *Computational Fluid Dynamics Incompressible Turbulent Flows*. Springer.
- KUMAR, B. & MITTAL, S. 2006 Prediction of the critical Reynolds number for flow past a circular cylinder. *Computer Methods in Applied Mechanics and Engineering* **195** (44–47), 6046–6058.
- KUNISCH, K. & VOLKWEIN, S. 2002 Galerkin proper orthogonal decomposition methods for a general equation in fluid dynamics. *SIAM Journal on Numerical analysis* **40** (2), 492–515.
- LE, H. & MOIN, P. 1991 An improvement of fractional step methods for the incompressible Navier-Stokes equations. *Journal of Computational Physics* **92** (2), 369–379.
- LEONARD, B. P. 1979 A stable and accurate convective modelling procedure based on quadratic upstream interpolation. *Computer Methods in Applied Mechanics and Engineering* **19** (1), 59–98.
- LUCHINI, P. & BOTTARO, A. 2014 Adjoint equations in stability analysis. *Annual Review of Fluid Mechanics* **46** (1), 493–517.
- LUMLEY, J. L. 1967 The structure of inhomogeneous turbulent flows. *Atmospheric turbulence and radio wave propagation* pp. 166–178.
- MA, X. & KARNIADAKIS, G. E. 2002 A low-dimensional model for simulating three-dimensional cylinder flow. *Journal of Fluid Mechanics* **458**, 181–190.
- MORLET, J., ARENS, G., FOURGEAU, E. & GLARD, D. 1982 Wave propagation and sampling theory—Part I: Complex signal and scattering in multilayered media. *Geophysics* **47** (2), 203–221.
- NAKAMURA, Y., SATO, S. & OHNISHI, N. 2024 Application of proper orthogonal decomposition to flow fields around various geometries and reduced-order modeling. *Computer Methods in Applied Mechanics and Engineering* **432**, 117340.
- NAKAMURA, Y., SATO, S. & OHNISHI, N. 2024, Kobe, Japan Reduced-order modeling for pressure field via global proper orthogonal decomposition. , vol. 12. Proceedings of Twelfth international conference on computational fluid dynamics.
- NAKAMURA, Y., SATO, S. & OHNISHI, N. 2025a Simulation method for finding a fixed point of Navier-Stokes equations by symmetricity constraints. *Under Review* .
- NAKAMURA, Y., SATO, S. & OHNISHI, N. 2025b Uncovering triadic interaction relationships latent in mode A behind a circular cylinder. *arXiv preprint arXiv:2504.00896* .
- NEKKANTI, A., PICKERING, E., SCHMIDT, O. T. & COLONIUS, T. 2025 Bispectral decomposition and energy transfer in a turbulent jet. *arXiv preprint arXiv:2502.15091* .
- NOACK, B. R., AFANASIEV, K., MORZYŃSKI, M., TADMOR, G. & THIELE, F. 2003 A hierarchy of low-dimensional models for the transient and post-transient cylinder wake. *Journal of Fluid Mechanics* **497**, 335–363.
- NOACK, B. R. & ECKELMANN, H. 1994a A global stability analysis of the steady and periodic cylinder wake. *Journal of Fluid Mechanics* **270**, 297–330.
- NOACK, B. R. & ECKELMANN, H. 1994b A low-dimensional Galerkin method for the three-dimensional flow around a circular cylinder. *Physics of Fluids* **6** (1), 124–143.
- NOACK, B. R., PAPAS, P. & MONKEWITZ, P. A. 2005 The need for a pressure-term representation in empirical Galerkin models of incompressible shear flows. *Journal of Fluid Mechanics* **523**, 339–365.
- OHMICHY, Y. 2014 Global linear stability analysis of compressible vortical flows. PhD thesis, Department of Advanced Energy, The University of Tokyo.
- OHMICHY, Y. 2024 Variational mode decomposition–based nonstationary coherent structure analysis for spatiotemporal data. *Aerospace Science and Technology* **149**, 109162.
- OHMICHY, Y. & YAMADA, K. 2021 Matrix-free triglobal adjoint stability analysis of compressible Navier–Stokes equations. *Journal of Computational Physics* **437**, 110332.
- RANJAN, R., UNNIKRISHNAN, S. & GAITONDE, D. 2020 A robust approach for stability analysis of complex flows using high-order Navier-Stokes solvers. *Journal of Computational Physics* **403**, 109076.
- RINOSHIKA, A. & RINOSHIKA, H. 2020 Application of multi-dimensional wavelet transform to fluid mechanics. *Theoretical and Applied Mechanics Letters* **10** (2), 98–115.
- ROLANDI, L. V., RIBEIRO, J. H. M., YEH, C.-A. & TAIRA, K. 2024 An invitation to resolvent analysis. *Theoretical and Computational Fluid Dynamics* **38** (5), 603–639.

- SAPSIS, T. P. & LERMUSIAUX, P. F. J. 2009 Dynamically orthogonal field equations for continuous stochastic dynamical systems. *Physica D: Nonlinear Phenomena* **238** (23–24), 2347–2360.
- SATO, S. & SCHMIDT, O. T. 2025 Parametric reduced-order modeling and mode sensitivity of actuated cylinder flow from a matrix manifold perspective. *arXiv preprint arXiv:2502.03754* .
- SCHMID, P. J. 2007 Nonmodal stability theory. *Annual Review of Fluid Mechanics* **39** (1), 129–162.
- SCHMID, P. J. 2010 Dynamic mode decomposition of numerical and experimental data. *Journal of fluid mechanics* **656**, 5–28.
- SCHMID, P. J. 2022 Dynamic mode decomposition and its variants. *Annual Review of Fluid Mechanics* **54** (1), 225–254.
- SCHMIDT, O. T. 2020 Bispectral mode decomposition of nonlinear flows. *Nonlinear Dynamics* **102** (4), 2479–2501.
- SCHMIDT, O. T. & COLONIUS, T. 2020 Guide to spectral proper orthogonal decomposition. *Aiaa journal* **58** (3), 1023–1033.
- SEN, S., MITTAL, S. & BISMAS, G. 2009 Steady separated flow past a circular cylinder at low Reynolds numbers. *Journal of Fluid Mechanics* **620**, 89–119.
- STANKIEWICZ, W., MORZYŃSKI, M., KOTECKI, K. & NOACK, B. R. 2017 On the need of mode interpolation for data-driven Galerkin models of a transient flow around a sphere. *Theoretical and Computational Fluid Dynamics* **31**, 111–126.
- TAIRA, K., BRUNTON, S. L., DAWSON, S. T., ROWLEY, C. W., COLONIUS, T., McKEON, B. J., SCHMIDT, O. T., GORDEYEV, S., THEOFILIS, V. & UKEILEY, L. S. 2017 Modal analysis of fluid flows: An overview. *AIAA Journal* **55** (12), 4013–4041.
- TAIRA, K., HEMATI, M. S., BRUNTON, S. L., SUN, Y., DURAISAMY, K., BAGHERI, S., DAWSON, S. T. & YEH, C.-A. 2020 Modal analysis of fluid flows: Applications and outlook. *AIAA Journal* **58** (3), 998–1022.
- TANEDA, S. 1959 Downstream development of the wakes behind cylinders. *Journal of the physical society of Japan* **14** (6), 843–848.
- TOWNE, A., SCHMIDT, O. T. & COLONIUS, T. 2018 Spectral proper orthogonal decomposition and its relationship to dynamic mode decomposition and resolvent analysis. *Journal of Fluid Mechanics* **847**, 821–867.
- TREFETHEN, L. N., TREFETHEN, A. E., REDDY, S. C. & DRISCOLL, T. A. 1993 Hydrodynamic stability without eigenvalues. *Science* **261** (5121), 578–584.
- TU, J. H. 2013 Dynamic mode decomposition: Theory and applications. PhD thesis, Princeton University.
- WILLIAMSON, C. H. K. 1996 Vortex dynamics in the cylinder wake. *Annual Review of Fluid Mechanics* **28** (1), 477–539.
- YAMADA, M. & OHKITANI, K. 1991 An identification of energy cascade in turbulence by orthonormal wavelet analysis. *Progress of Theoretical Physics* **86** (4), 799–815.
- YEUNG, B., CHU, T. & SCHMIDT, O. T. 2024 Revealing structure and symmetry of nonlinearity in natural and engineering flows. *arXiv preprint arXiv:2411.12057* .
- YEUNG, B. & SCHMIDT, O. T. 2025 Spectral dynamics of natural and forced supersonic twin-rectangular jet flow. *arXiv preprint arXiv:2501.10894* .
- ZHANG, H., ROWLEY, C. W., DEEM, E. A. & CATTAFESTA, L. N. 2019 Online dynamic mode decomposition for time-varying systems. *SIAM Journal on Applied Dynamical Systems* **18** (3), 1586–1609.
- ZHANG, W. & WEI, M. 2017 Model order reduction using DMD modes and adjoint DMD modes. In *8th AIAA Theoretical Fluid Mechanics Conference*, p. 3482.
- ZHONG, Y., AMIRI-MARGAVI, A., BABAEI, H. & TAIRA, K. 2025 Optimally time-dependent modes of vortex gust-airfoil interactions. *arXiv preprint arXiv:2501.02095* .